

# Understanding summertime peroxyacetyl nitrate (PAN) formation and its relation to aerosol pollution: Insights from high-resolution measurements and modeling

Baoye Hu<sup>1,3,4</sup>, Naihua Chen<sup>1,6</sup>, Rui Li<sup>7</sup>, Mingqiang Huang<sup>1,3,4</sup>, Jinsheng Chen<sup>2,5\*</sup>, Youwei Hong<sup>2,5</sup>, Lingling Xu<sup>2,5</sup>, Xiaolong Fan<sup>2,5</sup>, Mengren Li<sup>2,5</sup>, Lei Tong<sup>2</sup>, Qiuping Zheng<sup>8</sup>, Yuxiang Yang<sup>6\*</sup>

<sup>1</sup>College of Chemistry, Chemical Engineering and Environment, Minnan Normal University, Zhangzhou, China, 363000

<sup>2</sup>Center for Excellence in Regional Atmospheric Environment, Institute of Urban Environment, Chinese Academy of Sciences, Xiamen 361021, China

<sup>3</sup>Fujian Provincial Key Laboratory of Modern Analytical Science and Separation Technology, Minnan Normal University, Zhangzhou, China, 363000

<sup>4</sup>Fujian Province University Key Laboratory of Pollution Monitoring and Control, Minnan Normal University, Zhangzhou, China, 363000

<sup>5</sup>Fujian Key Laboratory of Atmospheric Ozone Pollution Prevention, Chinese Academy of Sciences, Xiamen 361021, China

<sup>6</sup>Pingtang Environmental Monitoring Center of Fujian, Pingtan 350400, China

<sup>7</sup>Key Laboratory of Geographic Information Science of the Ministry of Education, School of Geographic Science, East China Normal University, Shanghai 200241, PR China

<sup>8</sup>Xiamen Key Laboratory of Straits Meteorology, Xiamen Meteorological Bureau, Xiamen 361012, China

*Correspondence to:* Jinsheng Chen ([jschen@iue.ac.cn](mailto:jschen@iue.ac.cn)) & Yuxiang Yang ([907460293@qq.com](mailto:907460293@qq.com))

**Abstract:** Peroxyacetyl nitrate (PAN), a key indicator of photochemical pollution, is generated similarly to ozone (O<sub>3</sub>), through reactions involving specific volatile organic compounds (VOCs) and nitrogen oxides. Notably, PAN has been observed at unexpectedly high concentrations (maximum: 3.04 ppb) during the summertime. The daily maximum values of PAN showed a stronger correlation with black carbon (BC) (R=0.85) than with O<sub>3</sub> (R=0.75), suggesting a close connection between summertime haze and photochemical pollution. We addressed the puzzle of summertime PAN formation and its association with aerosol pollution under high O<sub>3</sub> conditions in Xiamen, a coastal city in southeastern China, by analyzing continuous high temporal resolution data utilizing box modeling in conjunction with the master chemical mechanism (MCM). The MCM model, with an index of agreement (IOA) value of 0.75, effectively investigate PAN formation, performing better during the clean period (R<sup>2</sup>: 0.68, slope K: 0.91) than haze one (R<sup>2</sup>: 0.47, slope K: 0.75). Using extreme gradient boosting (XGBoost), we identified NH<sub>3</sub>, NO<sub>3</sub><sup>-</sup>, and PM<sub>2.5</sub> as the primary factors for simulation bias. Moreover, the net production rate of PAN becomes negative with PAN constrained, suggesting

an unknown compensatory mechanism. Both relative incremental reactivity (RIR) and empirical kinetic modeling approach (EKMA) analyses indicate that PAN formation is VOC-controlled. Controlling emissions of VOCs, particularly alkenes, C<sub>5</sub>H<sub>8</sub>, and aromatics, would mitigate PAN pollution. PAN promotes OH and HO<sub>2</sub> while inhibiting the formation of O<sub>3</sub>, RO<sub>2</sub>, NO, and NO<sub>2</sub>. This study deepens our comprehension of PAN photochemistry while also offering scientific insights for guiding future PAN pollution control strategies.

## Introduction

PAN is a significant secondary gaseous pollutant commonly present in photochemical smog and poses risk to human health and plant growth, being 1-2 magnitudes more phytotoxic than O<sub>3</sub> (Yukihiro et al., 2012; Taylor, 1969). Additionally, PAN's low aqueous solubility, minimal reactivity with hydroxyl radicals (OH), and slow photolysis contribute to its capacity for long-range transport of nitrogen oxides (NO<sub>x</sub>) (Xu et al., 2018; Zhai et al., 2024; Marley et al., 2007b). Therefore, its formation in polluted areas holds significant importance beyond local concerns. Similar to surface O<sub>3</sub>, PAN is produced during the oxidation of VOCs in the presence of NO<sub>x</sub> (R1-R3) (Xu et al., 2021). PAN is formed when NO<sub>2</sub> reacts with peroxyacetyl (PA) radicals (CH<sub>3</sub>C(O)OO•) (R2), but the presence of NO consumes PA radicals, inhibiting PAN production (R3), which creates a comparable dependence of PAN and O<sub>3</sub> on NO and NO<sub>2</sub> levels. Unlike O<sub>3</sub>, however, PAN is influenced by only a limited number of oxygenated VOCs (OVOCs) that generate PA radicals. These OVOCs, which are second-generation precursors of PAN, include acetaldehyde (CH<sub>3</sub>CHO), acetone (CH<sub>3</sub>C(O)CH<sub>3</sub>), methylglyoxal (MGLY, CH<sub>3</sub>C(O)CHO), methyl vinyl ketone (MVK, CH<sub>2</sub>CHC(O)CH<sub>3</sub>), methyl ethyl ketone (MEK, CH<sub>3</sub>C(O)CH<sub>2</sub>CH<sub>3</sub>), methacrolein (MACR, CH<sub>2</sub>C(CH<sub>3</sub>)CHO), and biacetyl (CH<sub>3</sub>C(O)C(O)CH<sub>3</sub>). These compounds are typically formed from the oxidation of alkenes, aromatics, and isoprene, which are the first-generation precursors of PAN (Xue et al., 2014; Zhang et al., 2015). Identifying the dominant precursors is crucial for managing PAN pollution effectively. In the troposphere, thermal decomposition (R4) is the primary process responsible for PAN loss.



In recent years, wintertime photochemical air pollution has increasingly garnered attention. At this time, the concentration of O<sub>3</sub> is low due to the strong titration of NO, while the concentration of aerosol is high, and it is found that aerosol promotes PAN generation (Xu et al., 2021). Surprisingly high concentrations of OH radical, particularly under hazy conditions, have been observed and are largely attributed to HONO photolysis (Xu et al., 2021). Winter photochemical and haze pollution often exacerbate each other, with photochemical trace gases supplying both oxidants and precursors for aerosol formation, and aerosols acting as mediums for

60 heterogeneous reactions that produce key oxidants such as HONO, H<sub>2</sub>O<sub>2</sub>, and OH radicals (Xu et al., 2021). The OH produced by  
61 HONO photolysis can partially replace the UV action to promote PAN formation in winter in southeast coastal area of China when  
62 particulate matter is high ( $\geq 35 \mu\text{g}\cdot\text{m}^{-3}$ ) (Hu et al., 2020). Zhang et al. (2020) found the potential HONO sources significantly  
63 improved the PAN simulations in wintertime heavy haze events with high concentrations of PAN. High concentrations of PAN are  
64 a consequence of the increased levels of precursors and HONO observed during haze episodes (Liu et al., 2018). In conclusion,  
65 most previous studies have studied the effect of aerosol on PAN generation in winter. Further research on PAN should determine  
66 whether particulates significantly contribute to its formation during warmer seasons with elevated O<sub>3</sub> concentrations (Xu et al.,  
67 2021). In Eastern China, photochemical air pollution often involves high concentrations of both O<sub>3</sub> and PAN, a persistent issue  
68 during the warm season (April-September) for many years (Lu et al., 2020). The characteristics and formation pathways of PAN  
69 during summer have been increasingly studied in regions such as the North China Plain (NCP), the Yangtze River Delta, the Pearl  
70 River Delta, and southwestern China. These studies have generally shown consistent diurnal patterns and strong correlations  
71 between PAN and O<sub>3</sub>, identifying acetaldehyde—primarily derived from the degradation of aromatics and alkenes—as the key direct  
72 precursor of PAN in the summer. However, there has been limited research on the formation of PAN and its relationship with aerosol  
73 pollution during the summertime.

74 Xiamen is one of the fastest urbanizing regions in the southeast China and is also one of the cities with the best air quality in China,  
75 where the air quality could represent the future of other Chinese urban regions. Between 2018 and 2023, Xiamen ranked among the  
76 top 10 cities in China, achieving positions of 7th in 2018, 4th in both 2019 and 2020, 6th in 2021, 9th in 2022, and returning to 7th  
77 in 2023 (mcc.gov.cn, last assessed October 30, 2014). Xiamen is located in a low-latitude coastal area, with abundant sunlight and  
78 long daylight hours during the summer, resulting in strong solar radiation and rapid photochemical conversion rates. The city is  
79 typically influenced by the East Asian monsoon and serves as a transport channel for atmospheric pollutants from both the Yangtze  
80 River Delta and Pearl River Delta regions. Additionally, during the summer, Xiamen is often affected by complex meteorological  
81 conditions such as typhoons and the West Pacific Subtropical High (WPSH). The WPSH creates weather conditions that promote  
82 the formation and accumulation of photochemical pollutants and particulate matter (Wu et al., 2019). This setting provides an ideal  
83 "laboratory" for investigating the complexities of summertime PAN formation and its relationship with aerosol pollution under high  
84 O<sub>3</sub> concentrations. In summer, especially in July, high temperatures, high humidity, and intense radiation are likely to accelerate  
85 both the formation and consumption rates of PAN. In this study, continuous measurements of trace gases, substances related to  
86 aerosols, photolysis rate constants and meteorological parameters were performed at a suburban site in Xiamen from July 10th to  
87 July 31st, 2018. Firstly, we provide an overview of pollutant concentrations, meteorological parameters, and weather conditions  
88 during the observation period. Secondly, we simulate PAN concentration with the aid of box modeling combined with master  
89 chemical mechanism (MCM). Using machine learning with XGBoost, we identified the key factors that affect the observation-based  
90 model (OBM) model's simulation results and clarified the mechanisms linking haze pollution to photochemical air pollution, as

91 indicated by PAN and O<sub>3</sub>. Thirdly, the study identified the main precursors and oxidants responsible for summertime PAN production  
92 in Xiamen and evaluated the influence of PAN on local atmospheric oxidation capacity. This study further emphasized the interplay  
93 between haze and photochemical air pollution and highlighted significant implications for future research.

## 94 95 **2 Methodology**

### 96 **2.1 Field observations**

97 Trace gases (including PAN, O<sub>3</sub>, HONO, HNO<sub>3</sub>, HCl, NH<sub>3</sub>, VOCs, NO<sub>x</sub>, CO, and SO<sub>2</sub>), substances related to aerosols (including  
98 BC, PM<sub>1</sub>, PM<sub>2.5</sub>, PM<sub>10</sub>, SO<sub>4</sub><sup>2-</sup>, NO<sub>3</sub><sup>-</sup>, NH<sub>4</sub><sup>+</sup>, Cl<sup>-</sup>, Na<sup>+</sup>, K<sup>+</sup>, Ca<sup>2+</sup>, Mg<sup>2+</sup>), photolysis rate constants (including JO<sup>1</sup>D, JNO<sub>2</sub>, JHONO,  
99 JHCHO\_M, JHCHO\_R, JNO<sub>3</sub>\_M, JNO<sub>3</sub>\_R, JH<sub>2</sub>O<sub>2</sub>), and meteorological parameters (including temperature, relative humidity,  
100 atmospheric pressure, wind speed, and wind direction) were continuously measured at a suburban site in Xiamen from July 10th  
101 to July 31st, 2018. All instruments were placed inside an air-conditioned container situated on the rooftop of a 20-story building at  
102 the Institute of Urban Environment, Chinese Academy of Sciences (IUE: 118.06°E, 24.61°N) (Fig. S1(a)). When southerly winds  
103 prevailed, Xiamen Island, characterized by dense population and traffic congestion, was located upwind of the IUE (Fig. S1(b)).  
104 The IUE supersite is surrounded by Xinglin Bay, several universities and institutes, and major roadways with heavy traffic, such as  
105 Jimei Road (< 200 m), Shenhai Expressway (870 m), and Xiasha Expressway (2300 m) (Fig. S1(c)).

106 PAN measurements were conducted using a PANs-1000 analyzer (Focused Photonics Inc., Hangzhou, China), which features an  
107 automated system consists of a gas chromatograph, an electron capture detector, and a calibration unit. The analyzer provided PAN  
108 readings every 5 minutes, with a detection limit of 50 ppt. The uncertainty and precision of the PAN measurements were ±10% and  
109 3%, respectively. The PAN standard gas was produced through the reaction of acetone and NO under UV light. Calibration  
110 procedures included monthly multi-point calibrations and weekly single-point calibrations. Detailed information about the PAN  
111 detection system and calibration can be found in previous studies (Hu et al., 2020; Liu et al., 2022a). The VOC measurements were  
112 conducted using a gas chromatography mass spectrometer (GC-FID/MS, TH-300B, Wuhan, China) at an hourly time resolution.  
113 Detailed information regarding the VOC detection system and calibration procedures is available in our previous study (Liu et al.,  
114 2022b). HONO measurements were conducted using a customized Incoherent BroadBand Cavity Enhanced Absorption  
115 Spectroscopy (IBBCEAS) system developed by the Anhui Institute of Optics and Fine Mechanics (AIOFM), Chinese Academy of  
116 Sciences. The HONO detection limit was 100 ppt, with a time resolution of 1 minute. The measurement principle and calibration  
117 method of IBBCEAS can be found in the previous literature (Hu et al., 2022; Duan et al., 2018; Hu et al., 2024). The concentrations  
118 of inorganic components in PM<sub>2.5</sub> aerosols (including SO<sub>4</sub><sup>2-</sup>, NO<sub>3</sub><sup>-</sup>, NH<sub>4</sub><sup>+</sup>, Cl<sup>-</sup>, Na<sup>+</sup>, K<sup>+</sup>, Ca<sup>2+</sup>, Mg<sup>2+</sup>), as well as the concentrations of  
119 gases such as NH<sub>3</sub>, HCl, and HNO<sub>3</sub> were analyzed using a Monitor for AeRosols and Gases in ambient Air (MARGA, Model ADI  
120 2080, Applikon Analytical B.V., the Netherlands) (Hu et al., 2022). The criteria air pollutants O<sub>3</sub>, NO<sub>x</sub>, CO, and SO<sub>2</sub> were measured  
121 using different methods: ultraviolet (UV) absorption for O<sub>3</sub> (TEI model 49i), chemiluminescence with a molybdenum converter for

NO<sub>x</sub> (TEI model 42i), non-dispersive infrared for CO (TEI model 48i), and pulsed UV fluorescence for SO<sub>2</sub> (TEI model 43i). A tapered element oscillating microbalance (TEOM1405, Thermo Scientific Corp., MA, USA) was used to continuously measure the mass concentrations of PM<sub>1</sub>, PM<sub>2.5</sub>, and PM<sub>10</sub> online. A photolysis spectrometer (PFS-100, Focused Photonics Inc., Hangzhou, China) was employed to measure the photolysis rate constants. An ultrasonic anemometer (150WX, Airmar, USA) was used to measure meteorological parameters.

## 2.2 Box modeling

This study employed a box model framework utilizing the Master Chemical Mechanism (MCMv3.3.1, <https://mcm.york.ac.uk/MCM/home.htm>) to investigate sensitivity and mechanisms of PAN formation. The model constraints were derived from observations of trace gases and meteorological parameters, which were averaged to 1-hour intervals. The reliability of model simulation results is often assessed using the index of agreement (IOA), which ranges from 0 to 1, with a higher IOA signifying greater alignment between observed and simulated values. Note that the model simulation values at this time are not constrained by PAN. For specific formulas, please refer to the supplementary information (Eq. S1). Other formulas, including PAN production rates (P(PAN)), net production of PAN (Net (PAN)), and the RIR, are provided in the supplementary information (Eq. S2- Eq. S4).

The MCM simulates the nonlinear interaction between PAN and its precursors by altering the VOCs-to-NO<sub>x</sub> ratio across multiple scenarios, while keeping all other parameters fixed. In this study, a 20% step size was applied, reducing VOCs and NO<sub>x</sub> from 200% down to 0% to construct a scenario matrix. A total of 121 scenarios were generated to model the PAN production rate. The scenario representing the average VOCs and NO<sub>x</sub> mixing ratio during the sampling period was designated as the base case, with the remaining 120 scenarios created by systematically adjusting the VOC-to-NO<sub>x</sub> ratio. The output from these 121 simulations was used to construct isopleth diagrams depicting the relationship between VOCs, NO<sub>x</sub>, and PAN.

## 2.3 Machine Learning Model

To identify the key factors influencing the performance of the model simulation, the Machine Learning (ML) model was applied to establish the prediction model of bias between simulation of OBM and observation. XGBoost is a supervised boosting algorithm that reduces the risk of over-fitting, captures the nonlinear relationships among predictor variables, and solves numerous data science problems in a rapid and accurate way (Li et al., 2024). It has demonstrated high performance in O<sub>3</sub> studies in over China. As compared to other bagging tree models like random forest, XGBoost can handle more complex data while consuming fewer computing resources. To further improve the interpretability of the ML model, the feature importance of independent input variables in the XGBoost model is quantified using the Shaply Additive explanation (SHAP) approach (Lin et al., 2024). The SHAP calculates a value that represents the contribution of each feature to the model's outcome, which has been successfully applied in atmospheric environmental studies (Li et al., 2024; Lin et al., 2024). When the model was being adjusted, 90% of the data was used as the training

153 set, and 10% of the data was used as the test set. The hyperparameters were tuned using grid search and cross-validation method.  
154 Specifically, for a single hyperparameter, grid search was used to obtain its more appropriate value range, and for the combinations  
155 of hyperparameters, the whole training set was split into ten folds and then run a grid search over pre-adjusted combinations of  
156 hyperparameters by training nine folds and predicting on the one fold in cross-validation procedure. For key hyperparameters of  
157 XGBoost model, the number of trees was 100, learning rate was 0.1, max depth was 6. The model was trained and tested on hourly  
158 data during the whole observation and the established model was examined by coefficient of determination ( $R^2$ ) value, the root-  
159 mean-squared error (RMSE) and mean absolute error (MAE). The formulas of RMSE and MAE are provided in the supplementary  
160 information (Eq. S5 & Eq. S6). The performance of both models is illustrated in Fig. S3. The  $R^2$ , MAE, and RMSE for the training  
161 set are 0.90, 0.08, and 0.12, respectively, while the corresponding values for the test set are 0.77, 0.10, and 0.14, respectively. These  
162 statistical metrics indicate that the XGBoost model is promising for further analysis.

### 164 3. Results and discussion

#### 165 3.1 Overview of observation

166 The measured data of PAN, related trace gases and meteorological parameters at IUE over 10-31 July 2018 are documented in Fig.  
167 1. Combined with the synoptic situation shown in Fig. S4, the 8th typhoon of 2018, Typhoon Maria, made landfall on the morning  
168 of the 11th at Huangqi Peninsula in Lianjiang County, Fujian. Due to the influence of the typhoon's outer spiral rain bands, there  
169 was moderate to heavy rain on the 11th. Correspondingly, there was a noticeable decrease in ultraviolet radiation and the  
170 temperatures. Starting from the 12th, a WPSH strengthened and extended westward, exerting control over Xiamen. In the lower  
171 atmosphere, it was influenced by the eastward flow, resulting in predominantly cloudy weather. From the 16th to the 18th, the area  
172 was affected by the outer periphery of Typhoon Shan Shen, which formed on the 17th in the northeastern part of the South China  
173 Sea and moved westward, making landfall along the coast of Wancheng Town, Wanning City, Hainan Province in the early hours  
174 of the 18th. During this period, the city experienced strong winds with gusts reaching 5 to 6 on the Beaufort scale in the urban areas.  
175 At the same time, the concentration of various pollutants reached their lowest levels, and the daily variation patterns were less  
176 pronounced. From the 20th to the 21st, Xiamen experienced the influence of the peripheral descending airflow associated with  
177 Typhoon Ampil (which formed in the northwest Pacific Ocean around 8:00 P.M. on the 18th and moved northwest, making landfall  
178 along the coast of Chongming Island, Shanghai, around noon on the 22nd). During this period, there were fewer clouds and higher  
179 temperatures. From the 22nd to the 24th, the city was successively affected by the outer periphery of Typhoon Ampil and a tropical  
180 low-pressure system, resulting in occasional showers or thunderstorms. From the 25th to the 31st, a WPSH once again strengthened  
181 and controlled Xiamen. As a result, Xiamen experienced stable meteorological conditions, with light winds ( $w_s = 1.04 \text{ m}\cdot\text{s}$ ),  
182 persistently high temperatures (maximum daily average of  $37.82^\circ\text{C}$ ), and high relative humidity (maximum daily average of  
183 81.65%). These factors created an environment that favored the buildup of particulate matter and enhanced the photochemical

184 formation of O<sub>3</sub> and PAN (Wu et al., 2019). The maximum daily average of PM<sub>2.5</sub>, O<sub>3</sub> and PAN were 49.26 μg·m<sup>-3</sup>, 93.62 ppb, and  
185 1.37 ppb, respectively.

186 The phenomenon of simultaneous high levels of photochemical and particulate matter appears. Throughout the 22-days campaign,  
187 12 days (including July 11th, 13th, 21st to 23rd, and 25th to 31st) were observed with 1 h concentrations of PM<sub>2.5</sub> exceeding 35  
188 μg·m<sup>-3</sup>; 13 days (including July 11th, 13th, 15th, 20th to 23rd, and 26th to 31st) were observed with 5-min concentrations of PAN  
189 exceeding 1 ppb. The maximum concentration was recorded at 3.04 ppb (5-min data) at 11:09 local time of 13 July 2018. This  
190 concentration of PAN is comparable to the levels recorded at downwind of Guangzhou, southern China (3.9 ppb) (Wang et al., 2010),  
191 2.51 ppb in Nashville, U.S (Roberts et al., 2002). However, this value was significantly lower than heavily polluted areas in northern  
192 China in the summer, such as Beijing (9.34 ppb, (Xue et al., 2014)), Lanzhou (9.12 ppb, (Zhang et al., 2009)), and Jinan (13.47 ppb,  
193 (Liu et al., 2018)). This is likely because the higher summer temperatures in the southeastern coastal region are conducive to the  
194 thermal decomposition of PAN, and the precursor concentrations of PAN, including NO<sub>2</sub> and VOCs, are significantly lower in the  
195 studied area compared to those in the northern region. The concentration of alkanes is the highest, followed by alkenes, OVOCs and  
196 aromatics, while halogenated hydrocarbons and C<sub>5</sub>H<sub>8</sub> exhibit lower concentrations (Fig. S5). Furthermore, VOC concentrations for  
197 various species are elevated during haze periods compared to clean periods (Fig. S5). Throughout the observation period, the  
198 variations in O<sub>3</sub> and PAN were almost identical, but the maximum concentration of O<sub>3</sub> occurred at 3:00 p.m. on July 29<sup>th</sup> (114.12  
199 ppb). The correlation between the maximum daily values of PAN and BC is the strongest (R=0.85), followed by O<sub>3</sub> (R=0.75) (Fig.  
200 S6), suggesting that summertime haze and photochemical pollution were deeply connected.

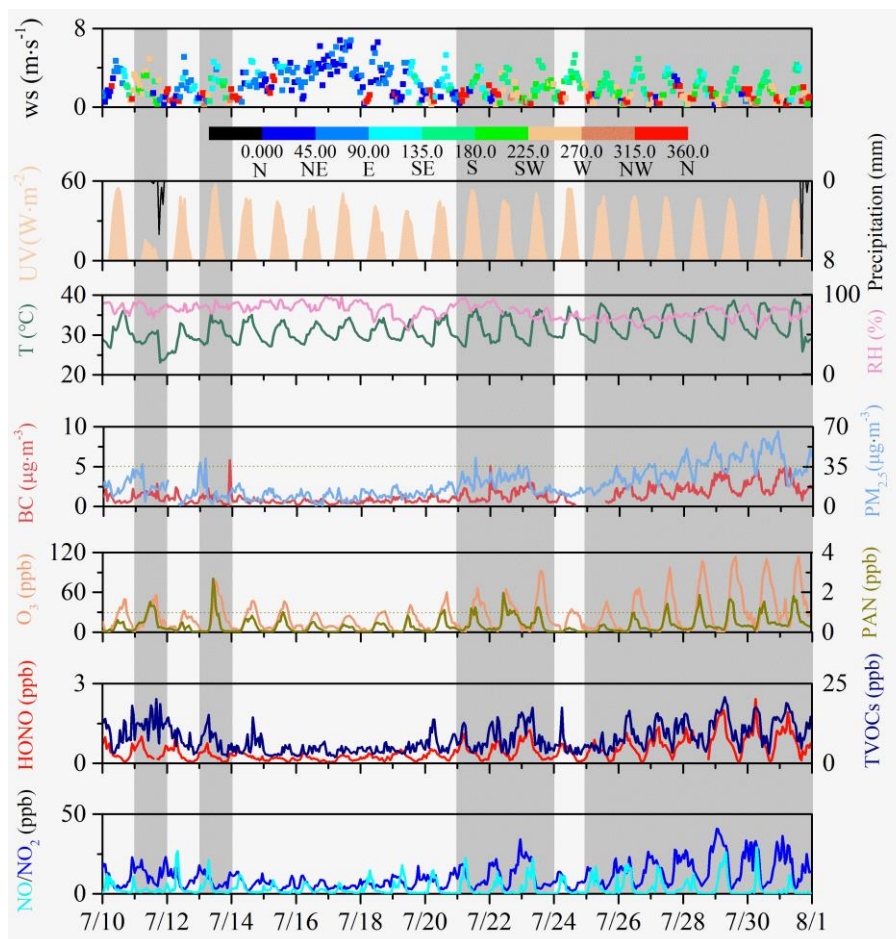


**Figure 1.** Time series of trace gases and meteorological parameters observed at IUE during 10-31 July 2018. The gray shading represents days when the PM<sub>2.5</sub> hourly daily maximum value exceeded 35  $\mu\text{g}\cdot\text{m}^{-3}$ .

We categorize it as "haze" and "clean" based on whether the PM<sub>2.5</sub> hourly daily maximum value is greater than 35  $\mu\text{g}\cdot\text{m}^{-3}$ . Specifically, "haze" includes July 11th, 13th, 21st to 23rd, and 25th to 31<sup>st</sup>, while other days are categorized as 'clean'. To provide a quantitative perspective, the statistics for PAN and associated species were calculated and compiled in Table 1. PM<sub>2.5</sub> concentrations during the haze period were significantly higher than those during the clean period, being 2.49 times those of the clean period. There was no significant difference of UV levels between clean and haze periods, while temperatures in the haze phase were notably higher than those in the clean phase. Therefore, without considering precursors, PAN concentrations should be lower during the haze phase due to higher thermal decomposition. In fact, PAN concentrations during the haze period were 2.35 times higher than those during the clean period. During the haze period, O<sub>3</sub> concentrations were also significantly higher than those during the clean period, being 2.04 times those of the clean period. These observations indicate that the atmospheric oxidation capacity is relatively strong during the haze period. Similar to PAN, HONO also exhibits higher concentrations during the haze phase (approximately 2.33 times that of clean conditions), which is consistent with current research findings that particles promote the generation of HONO (Ye et al., 2017). NO also experienced an increase from clean (3.28 ppb) to hazy (4.30 ppb) conditions, albeit less prominently than NO<sub>2</sub> (from 7.21 to 14.55 ppb). This observation further underscores that, during hazy periods, the



218 atmosphere demonstrates heightened oxidizing potential, facilitating the conversion of NO to NO<sub>2</sub>. While the increased NO levels  
 219 on hazy days reduced PA radicals and hindered PAN formation, this effect was offset by the concurrently higher concentrations of  
 220 PAN precursors (NO<sub>2</sub> and VOCs) during those days. The TVOCs have increased to some extent, but in hazy conditions, they are  
 221 only 1.34 times that of clean conditions. This is also because the strong oxidizing conditions during haze periods convert VOCs  
 222 into secondary pollutants, such as O<sub>3</sub> and PAN. Although it is acknowledged that VOCs can also be converted into secondary  
 223 organic aerosol (SOA), the discussion of SOA is beyond the scope of this study. The TVOC levels at this site are comparable to  
 224 that at a rural site in a coastal city-Qingdao (7.6 ppb), significantly lower than inland sites (such as Wuhan (30.2, (Liu et al., 2021a))  
 225 and Chengdu (28.0 ppb, (Yang et al., 2020))) or economically more developed coastal cities (such as Shanghai (25.3 ppb, (Zhu et  
 226 al., 2020)) and Hong Kong (26.9, (Wang et al., 2018))), and significantly higher than regional background locations like Mt. Wuyi  
 227 (4.7 ppb, (Hong et al., 2019)) and Mt. Nanling (4.7 ppb, (Wang et al., 2023)), and global background station Mt. Waliguan (2.6  
 228 ppb, (Xue et al., 2013)). The isoprene level during haze period was significantly higher than that during clean period probably due  
 229 to haze period with higher temperature (Wang et al., 2023). The wind speed was very low during both the clean and haze periods,  
 230 especially during the haze period with only 1.12 m·s<sup>-1</sup>. The relative humidity was high during both periods, and there was no  
 231 significant difference between the clean and haze periods.

232 **Table 1.** Descriptive statistics of major trace gases (ppb), particulate matter (μg·m<sup>-3</sup>) and meteorological parameters during 10-31  
 233 July 2018.

Species	Clean (mean ± SD)	Haze (mean ± SD)
PAN	0.20 ± 0.23	0.47 ± 0.46***
O <sub>3</sub>	16.07 ± 12.73	32.79 ± 29.73***
HONO	0.27 ± 0.18	0.63 ± 0.43***
NO	3.28 ± 4.03	4.30 ± 8.39***
NO <sub>2</sub>	7.21 ± 3.87	14.55 ± 8.89***
TVOCs	6.13 ± 1.73	8.19 ± 2.55***
C <sub>5</sub> H <sub>8</sub>	0.13 ± 0.04	0.17 ± 0.05***
PM <sub>1</sub>	10.13 ± 3.91	24.36 ± 10.77***
PM <sub>2.5</sub>	11.21 ± 5.33	27.93 ± 13.16***
PM <sub>10</sub>	24.26 ± 9.45	47.28 ± 20.63***
UV (W·m <sup>-2</sup> )	14.29 ± 17.38	13.18 ± 17.40
T (°C)	30.68 ± 2.39	31.92 ± 3.36***
RH (%)	81.94 ± 8.60	77.18 ± 8.22
WS (m·s <sup>-1</sup> )	1.64 ± 0.69	1.12 ± 0.61*

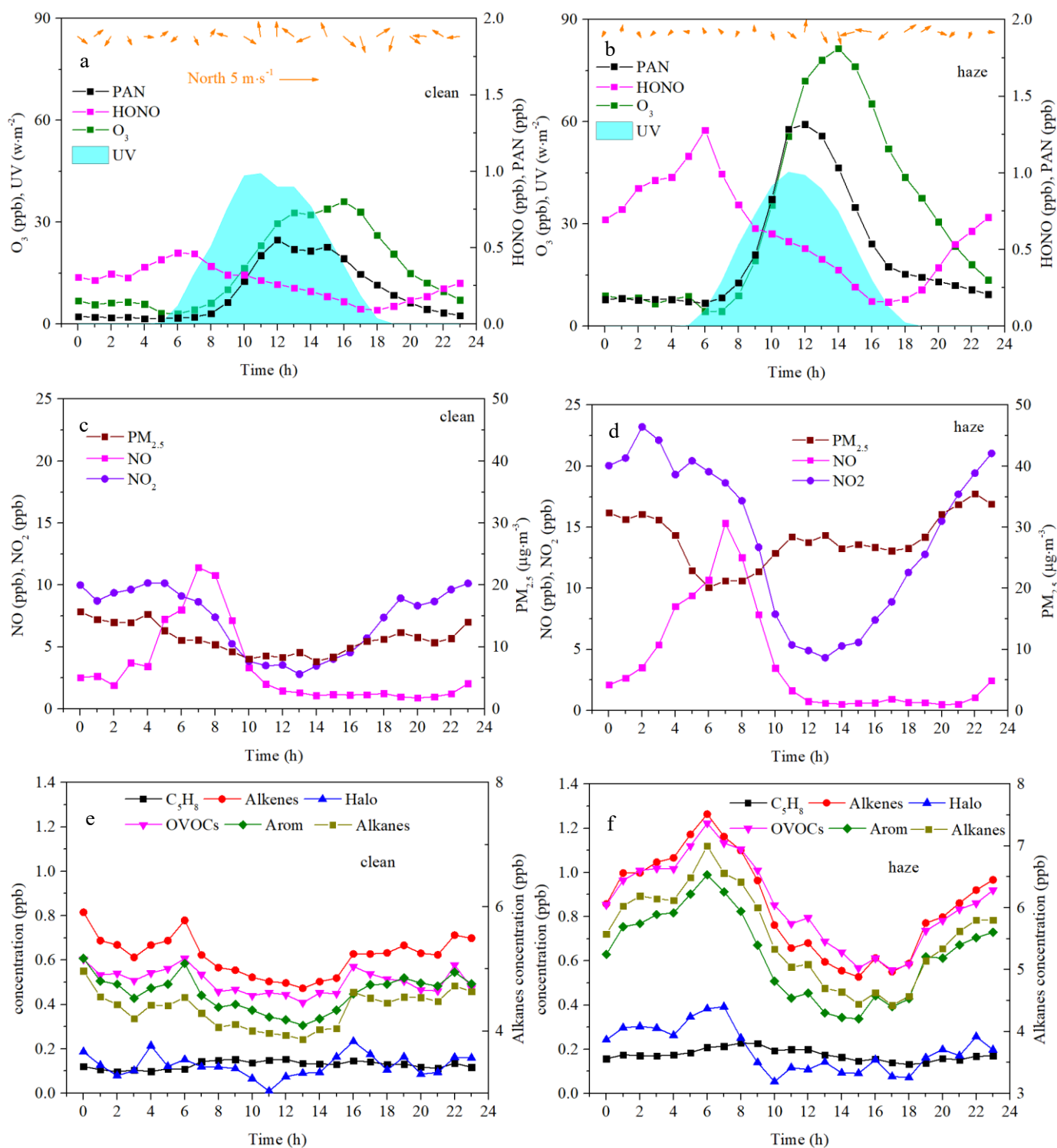
234 Note: \*, \*\*, and \*\*\* indicate that they passed the significance test at 0.05, 0.01 and 0.001 levels, respectively.

235  
 236 The average diurnal patterns of PAN and related variables have been averaged separately for clean and hazy conditions (Fig. 2).

237 The daily variation of PAN exhibits a clear unimodal pattern, with concentrations starting to rise after sunrise and decreasing after

238 12:00 caused by thermal decomposition of PAN at high temperatures (Fig. 2). Although PAN and O<sub>3</sub> exhibit a slight bimodal  
239 pattern during the clean period, this is primarily due to the bimodal pattern of UV during this time. The peak occurring at noon  
240 indicates that PAN primarily originates locally, as a delay of about 1-2 hours would be expected if it were influenced by  
241 transportation (Liu et al., 2024). The daytime increment was much larger for hazy condition ( $1.17 \pm 0.44$  ppb) than for clean  
242 condition ( $0.52 \pm 0.21$  ppb), indicating stronger photochemical production of PAN for hazy condition. The daily variation pattern  
243 of O<sub>3</sub> is similar to PAN, except that O<sub>3</sub> reaches its peak relatively later compared to PAN, with the peak occurring at 16:00 during  
244 the clean phase and 14:00 during the haze phase. Although PAN and O<sub>3</sub> are both products of photochemical reactions involving  
245 NO<sub>x</sub> and VOCs, their production efficiencies differ. PAN is specifically formed from VOCs that are precursors to the acetyl radical  
246 (CH<sub>3</sub>CO), whereas O<sub>3</sub> can be produced from the oxidation of any VOCs. Analyzing the correlation between PAN and O<sub>3</sub> can offer  
247 insights into their respective photochemical production efficiencies. As shown in Fig. S7, the positive correlation between the daily  
248 maximum values of PAN and O<sub>3</sub> for clean condition ( $R^2=0.6701$ ) was better than that for hazy condition ( $R^2=0.1504$ ). The slopes  
249 of the linear regression were 0.021 ppb/ppb for clean conditions and 0.009 ppb/ppb for hazy conditions. This indicates that, on  
250 average, approximately 2.1 ppb of PAN could be produced for each 100 ppb of O<sub>3</sub> formed under clean conditions, and about 0.9  
251 ppb of PAN for each 100 ppb of O<sub>3</sub> under hazy conditions in the air masses reaching IUE. The slope of linear regression for clean  
252 condition is comparable to those determined in Hongkong (0.028, (Xu et al., 2015)), Mexico city (0.02, (Marley et al., 2007a)),  
253 and Nashville (0.025, (Roberts et al., 2002)). The lower efficiency of PAN production relative to O<sub>3</sub> indicates that PAN precursors  
254 represent only a small portion of the total VOCs, especially during hazy conditions. Additionally, the high temperatures in the  
255 southeast coastal region likely contribute to the lower production efficiency of PAN. The average temperature during the entire  
256 observation period was 31.39 °C, with an average temperature of 34.64 °C at 12:00 LT. This result is consistent with the result that  
257 RIR during the cleaning period is higher than that during the haze period. As shown in Fig. S8, in the clean period, the correlation  
258 between PAN and O<sub>3</sub> is the strongest ( $R^2=0.70$ ), indicating that O<sub>3</sub> and PAN are both photochemical end products during clean  
259 periods. In contrast, during hazy periods, the correlation between PAN and O<sub>3</sub>×JO<sup>1</sup>D is the strongest ( $R^2=0.66$ ), suggesting that  
260 O<sub>3</sub> plays a more significant role in promoting PAN formation through photolysis to generate OH during hazy periods.  
261 Unlike the daily variation patterns of PAN and O<sub>3</sub>, HONO exhibits a swift concentration decrease after sunrise in both clean and  
262 hazy conditions, undergoing photolytic conversion into OH radicals. Subsequently, in clean conditions, HONO starts to increase  
263 in concentration after sunset. In hazy conditions, however, the increase begins from 16:00 LT and not after sunrise. This suggests  
264 a robust daytime net production or transport of HONO, where the rates surpass those of HONO photolysis and other sinks in the  
265 afternoon in hazy conditions. The NO levels reach their peak at 7:00 during the morning rush hour, reflecting advection of fresh  
266 urban plumes to the study site. The daily variation of NO<sub>2</sub> exhibits a 'U' shape, reaching its minimum value at 13:00, mainly owing  
267 to effects of emission, boundary layer height and photochemical reactions. In the clean period, the daily variation of PM<sub>2.5</sub> is  
268 similar to that of NO<sub>2</sub>, both showing a 'U' shape, reaching their lowest values at noon. However, during the haze phase, the daily

269 variation pattern of  $PM_{2.5}$  appears somewhat different. There is a noticeable trough in the early morning, remains stable during the  
 270 day, and starts to rise after sunset. The diurnal variation of VOC concentrations for various species are not significant during clean  
 271 periods (Fig. 2(e)), likely due to higher wind speeds that facilitate the dispersion of pollutants. In contrast, during haze periods, the  
 272 daily variations are evident, with peaks occurring before sunrise, followed by a decline, and then an increase after sunset (Fig.  
 273 2(f)). This is because the haze period is relatively stable at nighttime, which allows for the accumulation of pollutants, while during  
 274 the daytime, sunlight converts VOCs into photochemical products like  $O_3$  and PAN.



275

276

277

278

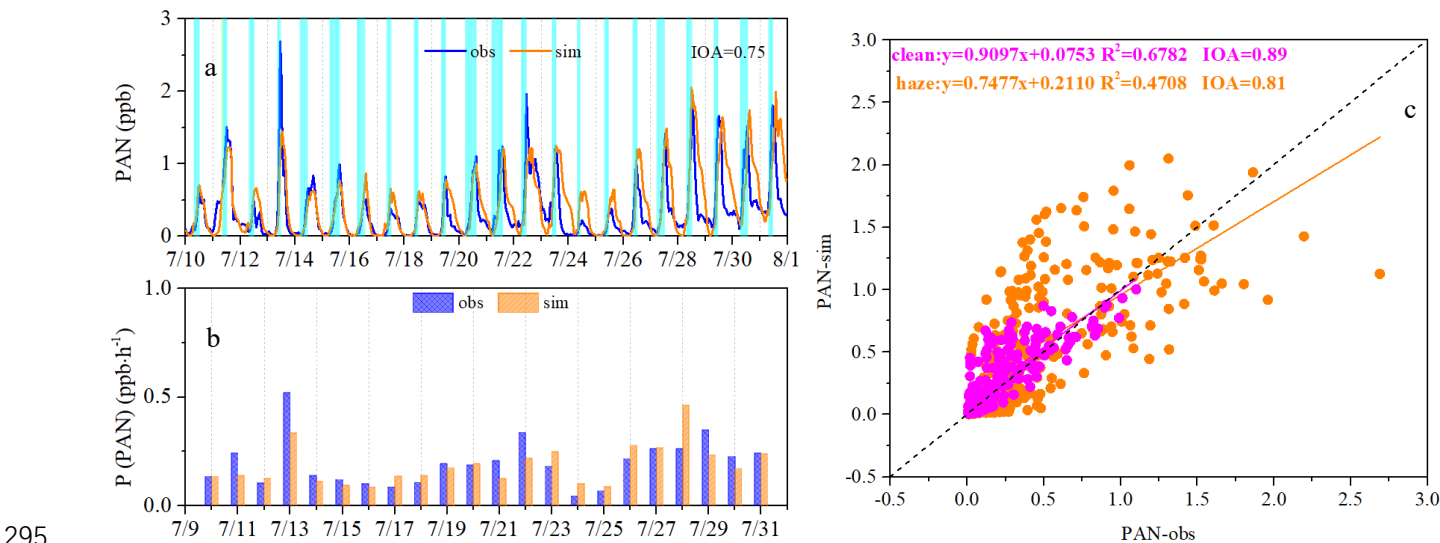
**Figure 2.** The diurnal variations of PAN, HONO,  $O_3$ , and UV during clean (a) and hazy (b) periods, the diurnal variations of  $PM_{2.5}$ ,

279 NO, and NO<sub>2</sub> during clean (c) and hazy (d) periods, and the diurnal variations of isoprene (C<sub>5</sub>H<sub>8</sub>), Alkenes, halogenated  
280 hydrocarbons (Halo), OVOCs, aromatics (Arom), and alkanes during clean (e) and hazy periods (f).

281

### 282 3.2 PAN formation: key factors and mechanisms

283 To investigate the key factors and mechanisms of PAN formation, PAN was simulated by constraining the MCM-based box model  
284 with meteorological conditions and observed concentrations of precursor gases. The model successfully replicated the variations  
285 in PAN, achieving an IOA of 0.75. (Fig. 3(a)), which was within the accepted range (0.66-0.87) in previous studies (Zeng et al.,  
286 2019). The model captured its formation rate well in general, with observed rates varying from 0.04 to 0.52 ppb·h<sup>-1</sup> (average: 0.20  
287 ppb·h<sup>-1</sup>) and modeled rates ranging from 0.09 to 0.46 ppb·h<sup>-1</sup> (average: 0.19 ppb·h<sup>-1</sup>) (see Fig. 3(b)). The similar result was found  
288 in the North China Plain (NCP) region in the wintertime (Xu et al., 2021). When calculating the IOA separately for clean and hazy  
289 periods, it was found that the IOA significantly increased to 0.89 and 0.81 (Fig. 3(c)), respectively. This phenomenon indicates a  
290 substantial difference in the PAN production and destruction mechanisms between clean and hazy periods. Furthermore, the  
291 simulated values are closer to the observed values during clean period, reflected in a higher R<sup>2</sup> value (R<sup>2</sup>=0.68) and a slope value  
292 (K) closer to 1 (K=0.91) (Fig. 3(c)). In contrast, the R<sup>2</sup> value and the K value during hazy period are only 0.47 and 0.75, respectively  
293 (Fig. 3(c)). This phenomenon suggests that some reactions related to PAN generation or destruction might be missing in the MCM  
294 during the hazy period.

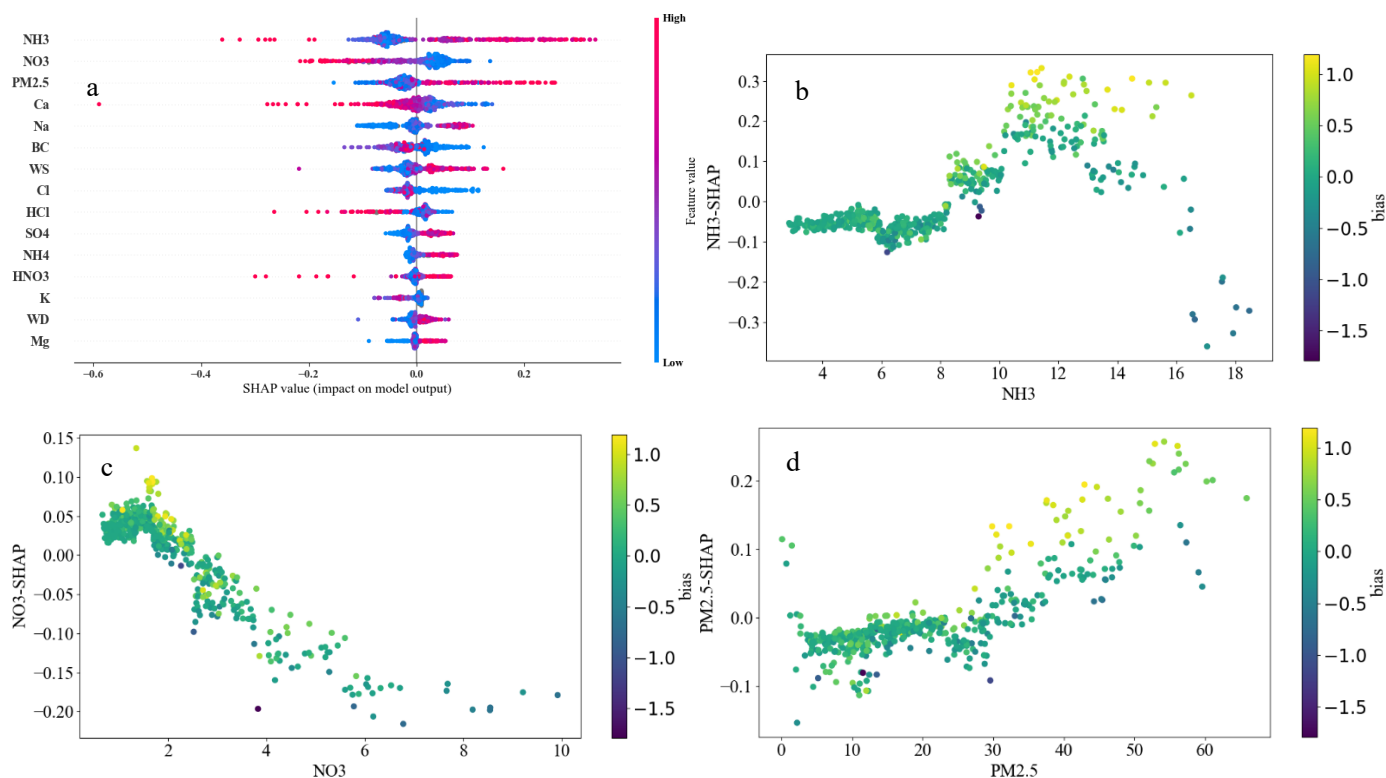


296 **Figure 3.** Comparisons of observed (obs) PAN and simulated (sim) PAN (daytime photochemical PAN production periods  
297 indicated by cyan shading), (b) production rates, (c) correlation between PAN observations and simulated values.

298

299 To identify the key factors influencing the performance of the OBM model simulation, the bias (the model simulation minus the  
300 observed value) as the target. The remaining variables, which were not input into the OBM model, such as NH<sub>3</sub>, HNO<sub>3</sub>, HCl  
301 (alkaline and acidic gaseous pollutants), PM<sub>2.5</sub> concentrations and their components, as well as physical process parameters like  
302 wind speed and wind direction, were used as features. As shown in Fig. 4 (a), through XGBoost-SHAP machine learning, we found

303 that  $\text{NH}_3$  is the most significant parameter affecting bias, contributing 19.68 % (Fig. S9). A scatter plot analysis of the SHAP values  
 304 of  $\text{NH}_3$  versus  $\text{NH}_3$  concentrations revealed that as  $\text{NH}_3$  concentrations increase (Fig. 4 (b)), the OBM model tends to overestimate  
 305 more significantly. To date, there are very few studies that directly address the impact of  $\text{NH}_3$  on PAN formation. Xu et al. (2021)  
 306 suggested that  $\text{NH}_3$  could promote the formation of HONO, which in turn affects PAN formation. However, since we included  
 307 HONO as an input to constrain the model, the indirect influence of  $\text{NH}_3$  on PAN formation through HONO can be excluded.  $\text{NH}_3$   
 308 in the atmosphere can preferentially react with sulfuric acid ( $\text{H}_2\text{SO}_4$ ) to form ammonium sulfate ( $(\text{NH}_4)_2\text{SO}_4$ ) secondary inorganic  
 309 aerosols (Behera et al., 2013), leading to the heterogeneous reaction removal of PAN by secondary inorganic aerosols (Pratap et  
 310 al., 2021). This result is validated by the positive correlation between the SHAP values of  $\text{NH}_4^+$  and  $\text{SO}_4^{2-}$  and their respective  
 311 concentrations (Fig. S10).  $\text{NO}_3^-$  is the second most significant parameter influencing the bias between the two, contributing 11.33 %  
 312 ((Fig. S9)).  $\text{NO}_3^-$  has a negative correlation with the bias (Fig. 4 (c)), indicating that higher  $\text{NO}_3^-$  levels lead to more significant  
 313 underestimation by the model. Considering the significant positive correlation between PAN and  $\text{NO}_3^-$  at the 0.01 level, with a  
 314 correlation coefficient of 0.37, and the fact that both reach their peaks around noon (Fig. S11), it is likely that they have a common  
 315 source.  $\text{PM}_{2.5}$  is the third most significant parameter (Fig. 4 (a)), contributing 9.40 % (Fig. S9).  $\text{PM}_{2.5}$  has a positive correlation  
 316 with the bias (Fig. 4 (d)), indicating that higher  $\text{PM}_{2.5}$  levels lead to more significant overestimation by the model, suggesting that  
 317 PAN can undergo heterogeneous removal on the surface of  $\text{PM}_{2.5}$  in the actual atmosphere (Sun et al., 2022).



318

319

320 **Figure 4.** Feature importance was obtained by XGBoost-SHAP method (a). The scatter plots between concentration of top three  
 321 important features and their SHAP values (b, c and d), and colored with the bias (the model simulation minus the observed value).  
 322

323

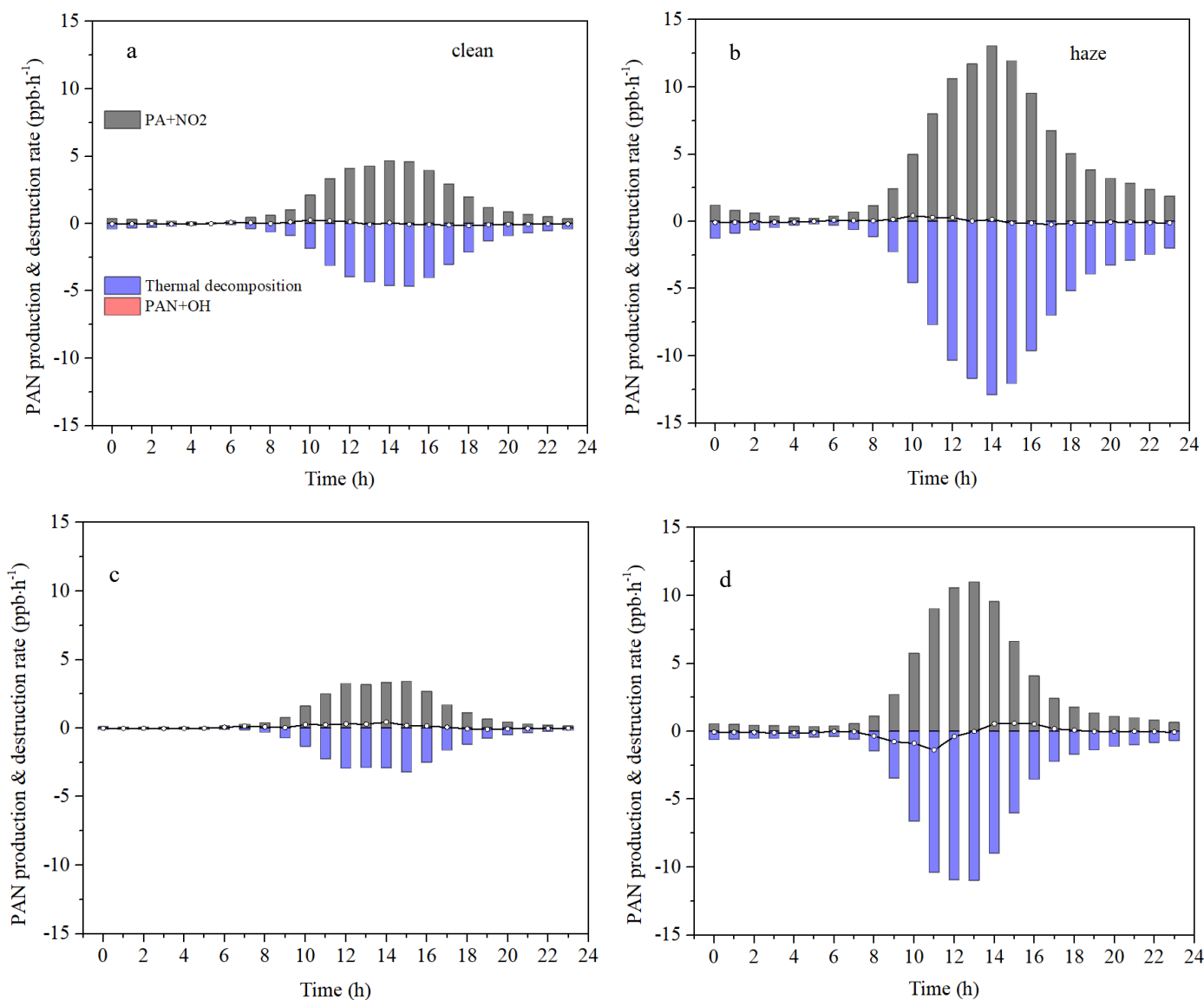
Figure 5 (a) and (b) show the average production and destruction rates of PAN during clean and haze periods, as simulated by

324 OBM without PAN constrained. During the haze period, both the production and destruction rates of PAN are significantly higher  
325 than during the clean period. The higher production rate of PAN during the haze period is due to the higher concentration of PAN  
326 precursors, while the higher destruction rate is because both the temperature and PAN concentration are higher. Regarding the net  
327 production rate, it is also higher during the haze period than during the clean period, which corresponds to the previously observed  
328 diurnal variation. From 6:00 to 12:00 during the haze period, the simulated net production rate of PAN is positive, with an average  
329 value of  $0.19 \text{ ppb}\cdot\text{h}^{-1}$ . During the clean period, from 6:00 to 12:00, the simulated net production rate of PAN is  $0.12 \text{ ppb}\cdot\text{h}^{-1}$ . The  
330 observed diurnal variation of PAN shows that from 6:00 to 12:00, the average net production rates during the haze and clean  
331 periods are  $0.20 \text{ ppb}\cdot\text{h}^{-1}$  (Fig. 2(a)) and  $0.09 \text{ ppb}\cdot\text{h}^{-1}$  (Fig. 2(b)), respectively. The model-simulated net production rate is close to  
332 the observed net production rate, further indicating that the model can simulate PAN well, and also confirming that PAN in summer  
333 mainly comes from local production. The net production rate of PAN during the haze period is similar to the summer results in  
334 urban areas of the Pearl River Delta (PRD), which is  $0.17 \text{ ppb}\cdot\text{h}^{-1}$ , while the net production rate of PAN during the clean period is  
335 similar to the summer results in rural areas of the PRD, which is  $0.12 \text{ ppb}\cdot\text{h}^{-1}$  (Liu et al., 2024).

336 Figure 5 (c) and (d) show the average production and destruction rates of PAN during clean and haze periods, as simulated by OBM  
337 with PAN constrained. The net production rate of PAN is approximately zero at night during both clean and haze periods, while  
338 there is a significant difference in the net production rate during the day. During the clean period, the daytime net production rate of  
339 PAN is greater than zero, with an average value of  $0.19 \text{ ppb}\cdot\text{h}^{-1}$ . In contrast, during the haze period, the net production rate of PAN  
340 is negative from 6 a.m. to 1 p.m., with an average value of  $-0.47 \text{ ppb}\cdot\text{h}^{-1}$ , and positive from 2 p.m. to 5 p.m., with an average value  
341 of  $0.47 \text{ ppb}\cdot\text{h}^{-1}$ . Previous research has shown that an increase in temperature, an increase in PAN concentration, or a decrease in  
342 PAN precursors (including VOCs and  $\text{NO}_2$ ) can cause the net production rate of PAN to change from positive to negative (Liu et al.,  
343 2024). We conducted a correlation analysis of the net production rate of PAN with temperature, PAN, VOCs, and  $\text{NO}_2$  concentration  
344 and found that the net production rate of PAN had the best correlation with PAN concentration ( $R^2=0.1316$ ), showing a significant  
345 negative correlation ( $k=-0.5283$ ) (Fig. S12). Additionally, we also observed that when the net production rate of PAN is negative,  
346 the PAN concentration is often very high (Fig. S12). As shown in Fig. 6, we conducted sensitivity experiments by reducing the PAN  
347 concentration by 80 %, i.e., 0.2 times the observed value, and found that the simulated net production rate of PAN was positive  
348 throughout the observation period. Conversely, when the PAN concentration was increased by 140%, i.e., 2.4 times the observed  
349 value, the simulated net production rate of PAN was found to be almost negative throughout the observation period. Besides, we  
350 also conducted sensitivity experiments on temperature and found that when simulating winter temperatures, i.e., 0.4 times the  
351 observed value, with a temperature range of  $9.25\text{-}15.29^\circ\text{C}$ , the simulated net production rate of PAN was positive throughout the  
352 observation period. Similarly, when simulating spring and autumn temperatures, i.e., 0.6 times the observed value, with a  
353 temperature range of  $13.87\text{-}23.39^\circ\text{C}$ , the simulated net production rate of PAN was also positive throughout the observation period.

354 In conclusion, the simulated net production rate of PAN becomes negative with PAN constrained, further suggesting the existence

355 of an unknown compensatory mechanism.

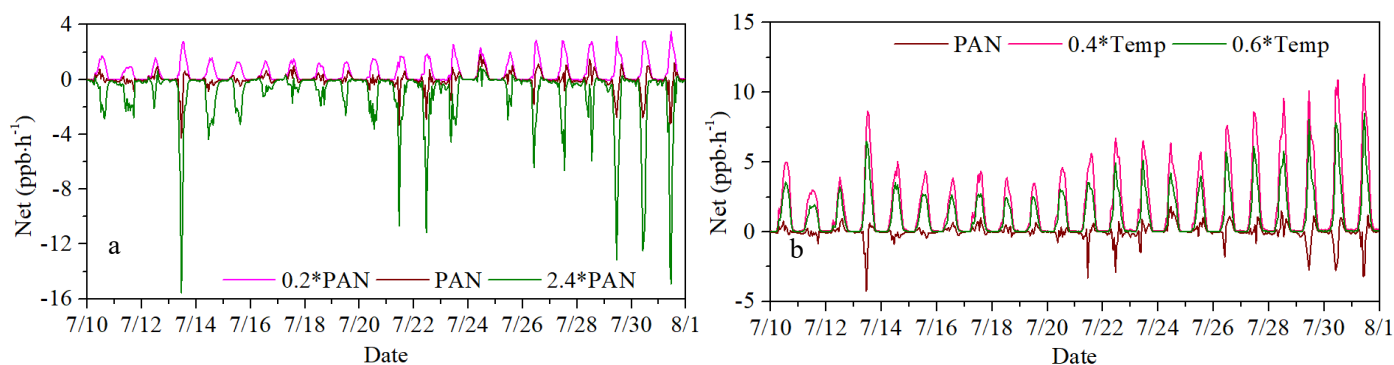


356

357

358 **Figure 5.** Average diurnal variation of the OBM simulated production, destruction and net rates of PAN during clean (a) and haze  
359 (b) without PAN constrained. And average diurnal variation of the OBM simulated production, destruction and net rates of PAN  
360 during clean (c) and haze (d) with PAN constrained.

361



362

363 **Figure 6.** Net PAN production rates simulated by OBM at different PAN concentrations (a) and different temperatures (b).

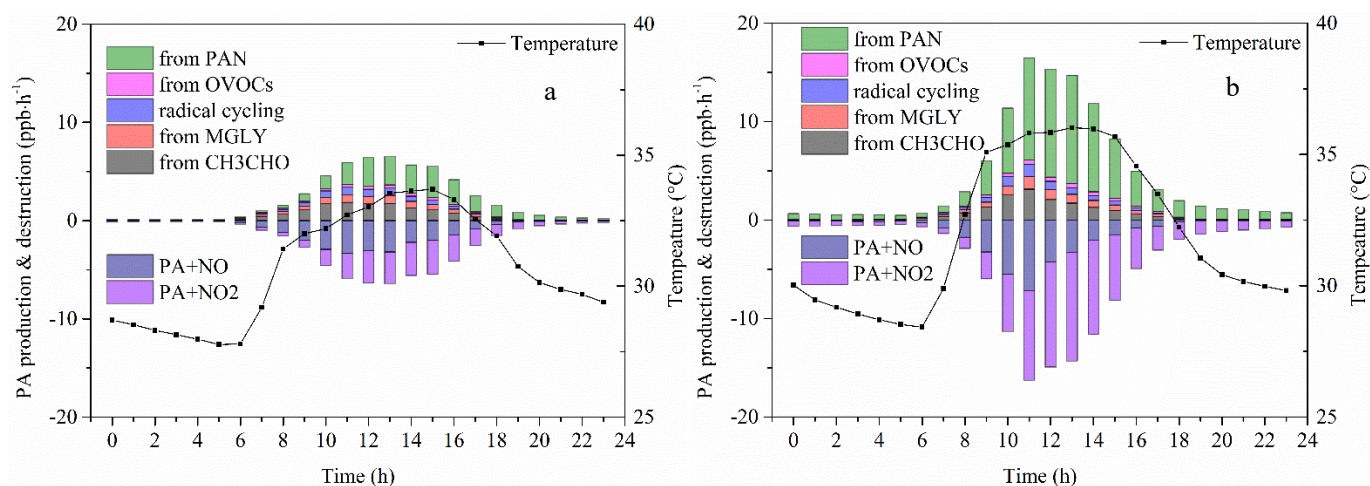
364

365 PAN is formed when the PA radical reacts with NO<sub>2</sub>. Given the swift equilibrium between R2 and R4 at high temperatures, budget  
366 analysis of PA's production and consumption pathways are frequently used to detail the mechanisms behind PAN formation (Sun et  
367 al., 2020; Liu et al., 2022a; Liu et al., 2024). Figure 7 illustrates the diurnal patterns of the primary production and loss pathways  
368 for the PA radical simulated by OBM across different periods. As shown in Fig. 7, during haze days, the rates of PA production and  
369 destruction were twice as high as those on clean days. This indicates that radical cycling and photochemical formation were more  
370 efficient during haze days, driven by higher temperatures and a greater abundance of precursors (Zeng et al., 2019). The PA radical  
371 production rate from PAN thermal decomposition reached its peak at 15:00 (3.22 ppb·h<sup>-1</sup>) and 13:00 (10.99 ppb·h<sup>-1</sup>) for clean and  
372 haze days, perfectly coinciding with the peak temperature time. In addition, the conversion of PAN into PA radical through thermal  
373 decomposition had high exponential correlations with temperature during both haze (R<sup>2</sup>=0.95) and clean days (R<sup>2</sup>=0.91) (Fig. S13).  
374 Previous laboratory experiments also indicated that the thermal decomposition of PAN is exponentially related to temperature (Cox  
375 & Roffey 1977; Senum et al., 1986; Tuazon et al., 1990). The conversion of PAN into PA radical through thermal decomposition  
376 during haze days was significantly higher than that during clean days, which was not only enhanced by higher temperature but also  
377 maintained by higher PAN concentration during haze days. The thermal decomposition of PAN to PA radical during the day (5:00-  
378 18:00 local time) accounted for 68.22 % and 45.59 % during haze and clean days, respectively. The pathways that did not account  
379 for the transformation between PA and PAN reached their peak around noon (11:00 local time), coinciding with the highest solar  
380 radiation and the most intense photochemical reactions, which has been observed in spring and autumn at the same site (Liu et al.,  
381 2022a).

382 Production rates of PA from other pathways related to precursors, including OVOCs, radical cycling, MGLY, and CH<sub>3</sub>CHO, showed  
383 single-peak patterns around noon, which suggested that the PA radical generated from these pathways was primarily increased by  
384 intense solar radiation at noontime (Sun et al., 2020). The average day PA radical production rates from CH<sub>3</sub>CHO via reactions with  
385 OH and NO<sub>3</sub> were 1.10 and 0.93 ppb·h<sup>-1</sup>, accounting for 48.85% and 49.35 % (exclude PAN thermal decomposition sources) during  
386 haze and clean days, respectively. These percentages were comparable to previous studies in Guangzhou (46 %) (Yuan et al., 2018)  
387 and Beijing (34.11-50.19 %) (Xue et al., 2014), suburban site of Chongqing (47.72 %) (Sun et al., 2020). The second production  
388 pathway involved MGLY undergoing photolysis and oxidation through reactions with OH and NO<sub>3</sub> (haze: 0.50 ppb·h<sup>-1</sup> and clean:  
389 0.42 ppb·h<sup>-1</sup>), contributing to 22.27 % and 22.12 % for haze and clean days, respectively. Subsequently, radical cycling processes—  
390 including the decomposition of RO radicals and the reactions of acyl peroxy radicals with NO—were also significant contributors  
391 to PA production, accounting for 18.98% on haze days and 19.54% on clean days. PA from the other OVOCs (excluding CH<sub>3</sub>CHO,  
392 MGLY) via photolysis and oxidation reactions involving OH, NO<sub>3</sub>, and O<sub>3</sub>, accounted for 9.90 % and 8.99% during haze (0.22  
393 ppb·h<sup>-1</sup>) and clean days (0.17 ppb·h<sup>-1</sup>). There were no notable differences in the proportions of individual pathways contributing to  
394 PA between haze and clean days, indicating comparable pollutant compositions in the atmospheric around IUE (Zeng et al., 2019).  
395 In summary, the thermal decomposition of PAN played the dominant role in boosting PA production rates during both clean and



396 haze periods, followed by contributions from CH<sub>3</sub>CHO, MGLY, radical cycling, and other OVOCs. The primary contributor to the  
 397 PA destruction rate was the reaction between PA and NO<sub>2</sub>, accounting for 67.72 % and 51.09 % during haze (4.74 ppb·h<sup>-1</sup>) and clean  
 398 days (1.76 ppb·h<sup>-1</sup>), respectively, followed by PA+NO, contributing to 32.28 % and 48.91 % during haze (2.26 ppb·h<sup>-1</sup>) and clean  
 399 days (1.69 ppb·h<sup>-1</sup>), respectively.



400

401

**Figure 7.** PA radical production and destruction pathways simulated by OBM on (a) clean days and (b) haze days.

402

403

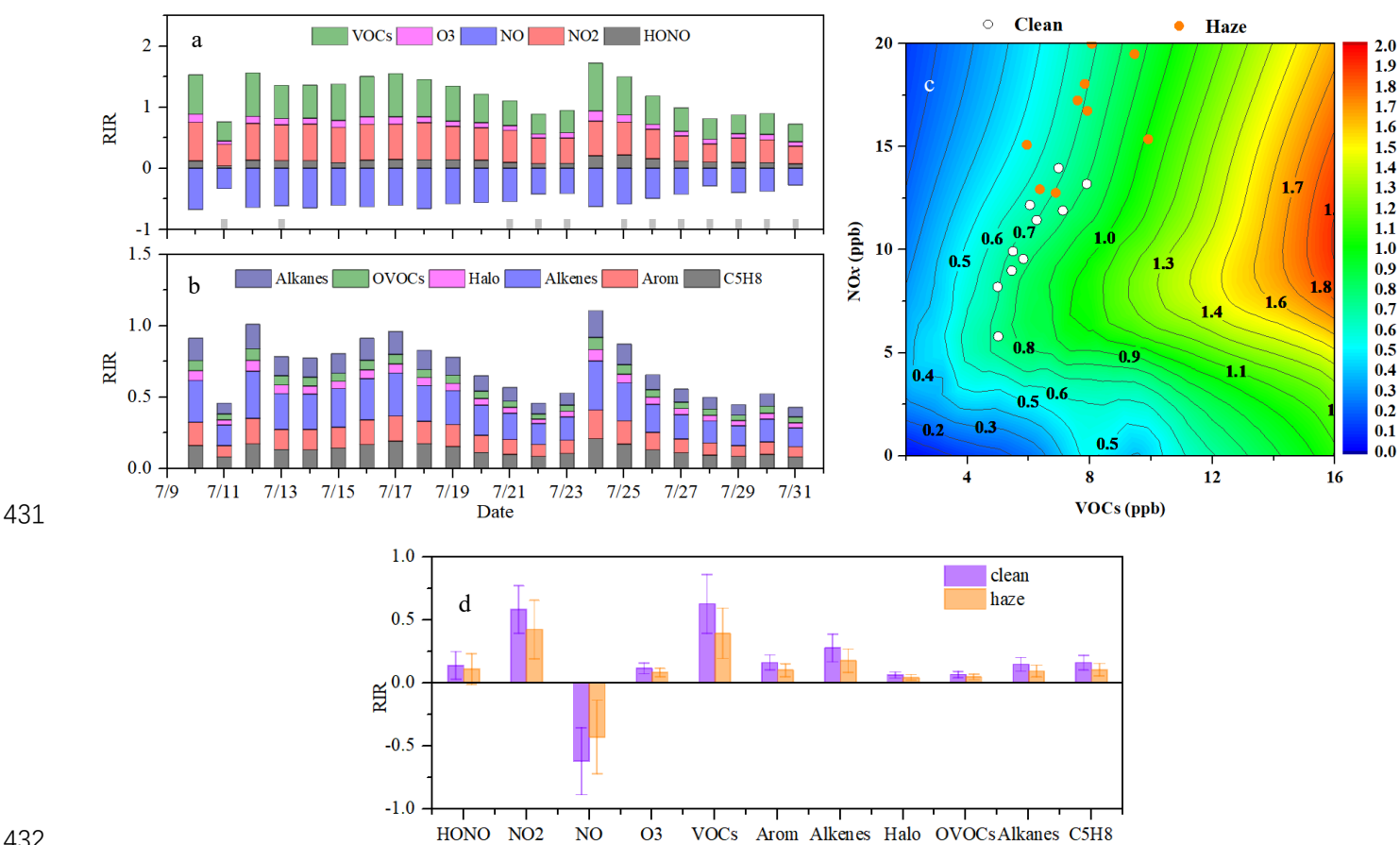
### 3.3 Sensitivity of PAN formation and its impact on the local atmosphere

404

To determine the principal precursors influencing PAN formation, sensitivity modeling analyses were carried out to investigate how PAN relates to its precursors. The RIR reflects how sensitive PAN formation is to changes in its precursor levels. As shown in Fig.8 (a), the RIR of NO was negative, ranging from -0.67 to -0.27 ( $-0.52 \pm 0.13$ ) throughout the observation period. However, RIR is positive for other species, with NO<sub>2</sub> ( $0.50 \pm 0.11$ ) and VOCs ( $0.50 \pm 0.15$ ) having the highest RIR, followed by HONO ( $0.12 \pm 0.04$ ) and O<sub>3</sub> ( $0.10 \pm 0.03$ ). Around 50 types of VOCs were classified as alkanes, OVOCs, halogenated hydrocarbons (Halo), alkenes, aromatics (Arom), and isoprene (C<sub>5</sub>H<sub>8</sub> representing biogenic hydrocarbons). Among these VOCs, the RIR of alkenes ( $0.22 \pm 0.07$ ) is the highest, followed by C<sub>5</sub>H<sub>8</sub> ( $0.13 \pm 0.04$ ) and Arom ( $0.13 \pm 0.04$ ), while OVOCs ( $0.06 \pm 0.01$ ) and Halo ( $0.05 \pm 0.01$ ) have very low RIRs (Fig. 8 (b)). These phenomena indicated that increased NO level would inhibit the production of PAN while increased NO<sub>2</sub>, VOCs (especially alkenes, C<sub>5</sub>H<sub>8</sub>, and Arom), HONO, and O<sub>3</sub> would promote the production of PAN. Because the values of NO and NO<sub>2</sub> RIR are approximately equal but with opposite signs, the RIR for NO<sub>x</sub> is almost zero, indicating that the PAN generation at this site is not sensitive to NO<sub>x</sub>. Zeng et al. (2019) also observed that NO<sub>2</sub> had a positive effect on PAN formation, while NO had a negative effect, in a suburban area of Hong Kong. This finding aligns with the fact that NO<sub>2</sub> directly contributes to PAN production, whereas NO reduces PA radicals, thereby inhibiting PAN formation. Based on the scenario analysis (Empirical Kinetic Modeling Approach (EKMA)), all data points for the 22 days fell above the ridge line (Fig. 8(c)). A reduction in VOCs at these points resulted in lower PAN concentrations, indicating that PAN formation at IUE was influenced by VOCs and thus VOC-sensitive. Our previous research also found that in this coastal city, PAN generation is limited by VOCs during the

419

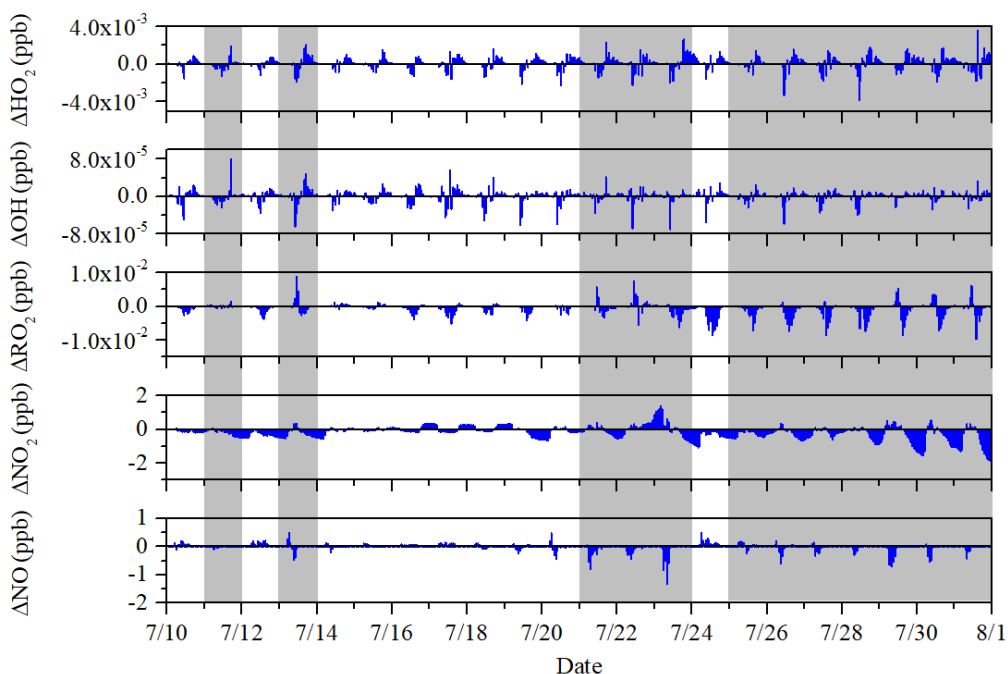
420 spring and autumn seasons. The difference is that previous studies indicated that reducing NO<sub>2</sub>, like reducing NO, also leads to an  
 421 increase in PAN concentration in spring and autumn (Liu et al., 2022a). This is because the NO<sub>x</sub> concentration in spring and autumn  
 422 is significantly higher than in summer, which is consistent with that both NO<sub>2</sub> and NO inhibit the formation of PAN in regions  
 423 with high NO<sub>x</sub> concentrations (Liu et al., 2024).  
 424 We divided the RIRs for different species into haze and clean periods and found that the RIRs during clean periods were consistently  
 425 higher than those during haze periods (Fig. 8(d)), which indicated that altering the concentrations of these species during clean  
 426 periods had a greater impact on PAN formation. The rapid thermal decomposition of PAN at high temperatures is likely the primary  
 427 reason. During the haze period, the main source of PA radical was PAN decomposition, which accounted for 68.22%, and the other  
 428 sources were smaller than that during the clean period (the source of the PA radical would be demonstrated in the following  
 429 paragraph). Therefore, the sensitivity of PAN production to precursors and HONO & O<sub>3</sub> producing OH became lower during the  
 430 haze period (Liu et al., 2021b; Liu et al., 2022a).



431  
 432  
 433 **Figure 8.** These four figures illustrate the RIR of PAN formation to major precursors (a), the impact of different VOCs species (b),  
 434 the isopleth diagrams of PAN formation (c), and a comparison of RIRs between clean and polluted periods (d).

435  
 436 As shown in Fig. 9,  $\Delta$ HO<sub>2</sub> and  $\Delta$ OH are positive for most periods, accounting for 72.16% and 70.83%, respectively, indicating that  
 437 the PAN mechanism promotes the generation of HO<sub>2</sub> and OH. Over the entire period,  $\Delta$ HO<sub>2</sub> is  $8.43 \times 10^{-5}$  ppb, with no significant  
 438 difference between clean and hazy periods, being  $8.18 \times 10^{-5}$  ppb and  $8.64 \times 10^{-5}$  ppb respectively (Table S1). OH behaves similarly,

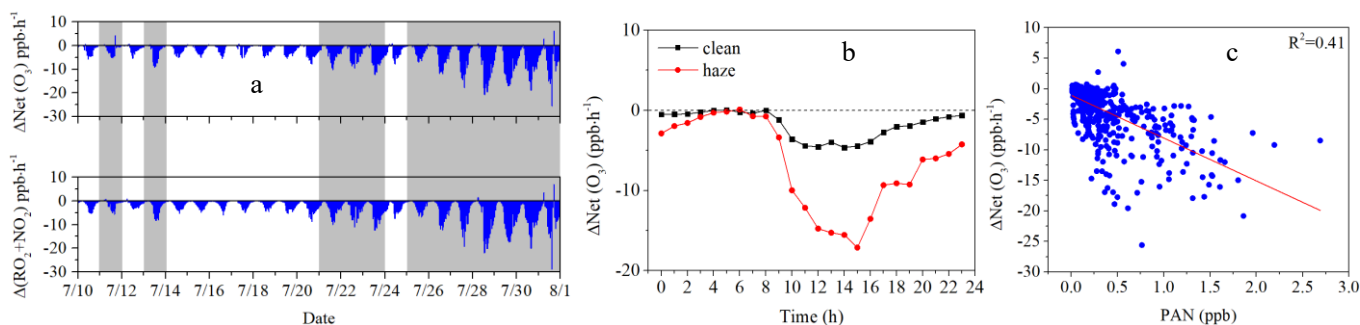
439 with  $\Delta\text{OH}$  being  $4.55 \times 10^{-7}$  ppb over the entire period, and also showing no significant difference between clean and hazy periods,  
 440 being  $4.94 \times 10^{-7}$  ppb and  $4.23 \times 10^{-7}$  ppb respectively (Table S1). The increase in simulated OH and HO<sub>2</sub> concentrations suggests that  
 441 PAN photochemistry is in favor of radical formation and atmospheric oxidative capacity at this site (Liu et al., 2024). Unlike HO<sub>2</sub>  
 442 and OH,  $\Delta\text{RO}_2$  and  $\Delta\text{NO}_2$  are negative for most periods, accounting for 53.22% and 67.23%, respectively, because PAN formation  
 443 uses up PA and NO<sub>2</sub>, the reduction in PA leads to a decrease in the amount of RO<sub>2</sub>. Over the entire period,  $\Delta\text{RO}_2$  is  $-6.4 \times 10^{-4}$  ppb,  
 444 with no significant difference between clean and hazy periods, being  $-6.11 \times 10^{-4}$  ppb and  $-6.55 \times 10^{-4}$  ppb respectively (Table S1).  
 445 The average value of  $\Delta\text{NO}_2$  during the entire observation period is -0.17 ppb respectively, with significant differences between hazy  
 446 and clean periods (Table S1). Specifically,  $\Delta\text{NO}_2$  is -0.22 during hazy periods and only -0.11 during clean periods, indicating that  
 447 the PAN mechanism consumes more NO<sub>2</sub> during hazy periods. Although  $\Delta\text{NO}$  is positive for most periods, accounting for 78.79%,  
 448 the overall mean is -0.01, with significant differences between hazy and clean periods (Table S1).  $\Delta\text{NO}$  is -0.05 during hazy periods,  
 449 showing an inhibitory effect, while it is 0.03 during clean periods, showing a promoting effect.



450  
 451 **Figure 9.** The time series of  $\Delta\text{HO}_2$ ,  $\Delta\text{OH}$ ,  $\Delta\text{RO}_2$ ,  $\Delta\text{NO}_2$ , and  $\Delta\text{NO}$ . The  $\Delta\text{HO}_2$ ,  $\Delta\text{OH}$ ,  $\Delta\text{RO}_2$ ,  $\Delta\text{NO}_2$ , and  $\Delta\text{NO}$  is calculated as the  
 452 base scenario with the PAN mechanism minus the scenario without the PAN mechanism.

453  
 454 As shown in Fig.10 (a), the PAN mechanism inhibited 85.80% of net O<sub>3</sub> production during the entire observation period, with  
 455 inhibition rates (the percentage of negative  $\Delta\text{Net}(\text{O}_3)$ ) of 83.75% and 87.50% during clean and haze periods, respectively. This  
 456 result is consistent with previous spring observations at the same site, where the inhibition rate was 83% (Liu et al., 2022a). The  
 457 PAN mechanism mainly inhibits the net O<sub>3</sub> generation by increasing the RO<sub>2</sub>+NO<sub>2</sub> reaction (Fig.10(a)), with negligible impact from  
 458 other reactions (Fig. S14). As shown in Fig.10(b), the diurnal variation trend indicates that the PAN mechanism's inhibitory effect  
 459 on O<sub>3</sub> is significantly greater during haze periods than during clean periods. Additionally, regardless of whether it is during haze

460 periods or clean periods, the PAN mechanism's inhibitory effect on  $O_3$  is significantly greater during the day than at night. These  
 461 phenomena all indicate that the higher the PAN concentration, the more pronounced the inhibitory effect of the PAN mechanism on  
 462  $O_3$  (Fig.10(c)). Under the condition of low precursors (including  $NO_x$  and VOCs) conditions, competition among these precursors  
 463 may limit their secondary transformation, thus resulting in inhibition (Liu et al., 2024).



464  
 465 **Figure 10.** (a) Time series plot of  $\Delta Net(O_3)$  and the reaction of  $\Delta(RO_2+NO_2)$ , (b) Diurnal variation of  $\Delta Net(O_3)$  during clean and  
 466 hazy conditions, (c) Correlation between  $\Delta Net(O_3)$  and PAN.  $\Delta Net(O_3)$  and  $\Delta(RO_2+NO_2)$  are calculated as the base scenario with  
 467 the PAN mechanism minus the scenario without the PAN mechanism.

## 468 Conclusion

469  
 470 This study thoroughly investigated the summertime PAN formation mechanism and established its connection to haze pollution. In  
 471 addition to  $NO$  and TVOCs, the concentration of all pollutants during the haze period is above twice that during the cleaning period,  
 472 indicating that the oxidation of  $NO$  and TVOCs during the haze period is stronger, which is conducive to the oxidation of  $NO$  and  
 473 TVOCs into secondary pollutants, such as  $O_3$  and PAN. The slopes of linear regression between the daily maximum values of PAN  
 474 and  $O_3$  were 0.021 ppb/ppb and 0.009 ppb/ppb for clean and hazy condition, respectively, implies that PAN precursors accounted  
 475 for only a small fraction of the total VOCs, especially for hazy condition. High temperature should be another factor contributing  
 476 to the lower production efficiency of PAN in the southeast coastal region. During the whole observation period, the IOA=0.75,  
 477 indicating that the MCM model is well-suited for exploring the photochemical formation of PAN. During the clean period,  
 478 simulation results were better than during the haze period ( $R^2$ : 0.68 vs. 0.47, slope K: 0.91 vs. 0.75), indicating that some reactions  
 479 related to PAN generation or destruction might be missing in the MCM during the hazy period. Additionally, the simulated net  
 480 production rate of PAN becomes negative with PAN constrained. However, the observed increasing in PAN concentrations indicates  
 481 that the actual net production rate is positive, suggesting that there are additional sources contributing to PAN generation that are  
 482 not considered in the MCM mechanism. Through XGBoost-SHAP machine learning, and given the significant positive correlation  
 483 between PAN and  $NO_3^-$  ( $R=0.37$ ) at the 0.01 level, and their peak around noon, they likely share a common source. Both RIR and  
 484 EKMA indicate that PAN formation in this region is VOC-controlled. Controlling emissions of VOCs, particularly alkenes,  $C_5H_8$ ,  
 485 and aromatics, would be beneficial for mitigating PAN pollution. The RIR results also show that during the clean period, PAN is  
 486 more sensitive to changes in various pollutants than during the haze period, highlighting the significant importance of deep emission

487 reductions. PAN presented the promotion effects on OH and HO<sub>2</sub>, while inhibited O<sub>3</sub> formation, RO<sub>2</sub>, NO and NO<sub>2</sub>. This study  
488 improves our thorough understanding of PAN photochemistry and offers valuable scientific guidance for the future management of  
489 PAN pollution.

#### 490 **Data availability**

491 The observation data at this site are available from the authors upon request.

#### 492 **Authorship Contribution Statement**

493 **Baoye Hu**: Methodology, Formal analysis, Investigation, Data curation, Writing – original draft. **Naihua Chen**: Software, Formal  
494 analysis. **Rui Li**: Software, Formal analysis. **Mingqiang Huang**: Software. **Jinsheng Chen**: Funding acquisition, Supervision,  
495 Writing - Review & Editing. **Youwei Hong**: Formal analysis. **Lingling Xu**: Investigation. Xiaolong Fan: Investigation. **Mengren**  
496 **Li**: Investigation. **Lei Tong**: Investigation. **Qiuping Zheng**: Investigation. **Yuxiang Yang**: Writing - Review & Editing

#### 497 **Competing interests**

498 The authors declare that they have no conflict of interest.

#### 499 **Acknowledgments**

500 This work was supported by the National Natural Science Foundation of China (grant nos. 42305102, U22A20578), Natural Science  
501 Foundation of Fujian Province (grant nos. 2023J05179), Natural Science Foundation of Zhangzhou City (grant nos. ZZ2023J07),  
502 Fujian Provincial Department of Education (grant nos. JAT210279), the Fund of Minnan Normal University President (grant nos.  
503 KJ2021009). This study was funded by Xiamen Atmospheric Environment Observation and Research Station of Fujian Province,  
504 and Fujian Key Laboratory of Atmospheric Ozone Pollution Prevention (Institute of Urban Environment, Chinese Academy of  
505 Sciences).

#### 506 **Supplementary information**

507 Attached please find supplementary information associated with this article.

508 **Reference**

- 509 Behera, S. N., Sharma, M., Aneja, V. P., and Balasubramanian, R.: Ammonia in the atmosphere: a review on emission sources,  
510 atmospheric chemistry and deposition on terrestrial bodies, *Environ. Sci. Pollut. Res.*, 20, 8092-8131, 10.1007/s11356-013-  
511 2051-9, 2013.
- 512 Cox, R. A., & Roffey, M. J. : Thermal decomposition of peroxyacetyl nitrate in the presence of nitric oxide. *Environ. Sci. Tech.*, 11,  
513 900-906, 10.1021/es60132a010, 1977.
- 514 Duan, J., Qin, M., Ouyang, B., Fang, W., Li, X., Lu, K., Tang, K., Liang, S., Meng, F., Hu, Z., Xie, P., Liu, W., and Häsel, R.:  
515 Development of an incoherent broadband cavity-enhanced absorption spectrometer for in situ measurements of HONO and  
516 NO<sub>2</sub>, *Atmos. Meas. Tech.*, 11, 4531-4543, 10.5194/amt-11-4531-2018, 2018.
- 517 Hong, Z., Li, M., Wang, H., Xu, L., Hong, Y., Chen, J., Chen, J., Zhang, H., Zhang, Y., Wu, X., Hu, B., and Li, M.: Characteristics  
518 of atmospheric volatile organic compounds (VOCs) at a mountainous forest site and two urban sites in the southeast of China,  
519 *Sci. Total Environ.*, 657, 1491-1500, 10.1016/j.scitotenv.2018.12.132, 2019.
- 520 Hu, B., Liu, T., Hong, Y., Xu, L., Li, M., Wu, X., Wang, H., Chen, J., and Chen, J.: Characteristics of peroxyacetyl nitrate (PAN) in  
521 a coastal city of southeastern China: Photochemical mechanism and pollution process, *Sci. Total Environ.*, 719,  
522 10.1016/j.scitotenv.2020.137493, 2020.
- 523 Hu, B., Wang, Y., Chen, J., Chen, N., Hong, Y., Xu, L., Fan, X., Li, M., and Tong, L.: The observation of atmospheric HONO by  
524 wet-rotating-denuder ion chromatograph in a coastal city: Performance and influencing factors, *Environ. Pollut.*, 356,  
525 10.1016/j.envpol.2024.124355, 2024.
- 526 Hu, B., Duan, J., Hong, Y., Xu, L., Li, M., Bian, Y., Qin, M., Fang, W., Xie, P., and Chen, J.: Exploration of the atmospheric chemistry  
527 of nitrous acid in a coastal city of southeastern China: results from measurements across four seasons, *Atmos. Chem. Phys.*,  
528 22, 371-393, 10.5194/acp-22-371-2022, 2022.
- 529 Li, H., Yang, Y., Su, H., Wang, H., Wang, P., and Liao, H.: Ozone pollution in China affected by climate change in a carbon neutral  
530 future as predicted by a process-based interpretable machine learning method, *Geophys. Res. Lett.*, 51, 10.1029/2024gl109520,  
531 2024.
- 532 Lin, Z., Xu, L., Yang, C., Chen, G., Ji, X., Li, L., Zhang, K., Hong, Y., Li, M., Fan, X., Hu, B., Zhang, F., and Chen, J.: Trends of  
533 peroxyacetyl nitrate and its impact on ozone over 2018–2022 in urban atmosphere, *Npj Clim. Atmos. Sci.*, 7, 10.1038/s41612-  
534 024-00746-7, 2024.
- 535 Liu, L., Wang, X., Chen, J., Xue, L., Wang, W., Wen, L., Li, D., and Chen, T.: Understanding unusually high levels of peroxyacetyl  
536 nitrate (PAN) in winter in Urban Jinan, China, *J. Environ. Sci.*, 71, 249-260, 10.1016/j.jes.2018.05.015, 2018.
- 537 Liu, T., Chen, G., Chen, J., Xu, L., Li, M., Hong, Y., Chen, Y., Ji, X., Yang, C., Chen, Y., Huang, W., Huang, Q., and Wang, H.:  
538 Seasonal characteristics of atmospheric peroxyacetyl nitrate (PAN) in a coastal city of Southeast China: Explanatory factors

539 and photochemical effects, *Atmos. Chem. Phys.*, 22, 4339-4353, 10.5194/acp-22-4339-2022, 2022a.

540 Liu, T., Hong, Y., Li, M., Xu, L., Chen, J., Bian, Y., Yang, C., Dan, Y., Zhang, Y., Xue, L., Zhao, M., Huang, Z., and Wang, H.:  
541 Atmospheric oxidation capacity and ozone pollution mechanism in a coastal city of southeastern China: analysis of a typical  
542 photochemical episode by an observation-based model, *Atmos. Chem. Phys.*, 22, 2173-2190, 10.5194/acp-22-2173-2022,  
543 2022b.

544 Liu, T., Wang, Y., Cai, H., Wang, H., Zhang, C., Chen, J., Dai, Y., Zhao, W., Li, J., Gong, D., Chen, D., Zhai, Y., Zhou, Y., Liao, T.,  
545 and Wang, B.: Complexities of peroxyacetyl nitrate photochemistry and its control strategies in contrasting environments in  
546 the Pearl River Delta region, *Npj Clim. Atmos. Sci.*, 7, 10.1038/s41612-024-00669-3, 2024.

547 Liu, X., Guo, H., Zeng, L., Lyu, X., Wang, Y., Zeren, Y., Yang, J., Zhang, L., Zhao, S., Li, J., and Zhang, G.: Photochemical ozone  
548 pollution in five Chinese megacities in summer 2018, *Sci. Total Environ.*, 801, 149603, 10.1016/j.scitotenv.2021.149603,  
549 2021a.

550 Liu, Y., Shen, H., Mu, J., Li, H., Chen, T., Yang, J., Jiang, Y., Zhu, Y., Meng, H., Dong, C., Wang, W., and Xue, L.: Formation of  
551 peroxyacetyl nitrate (PAN) and its impact on ozone production in the coastal atmosphere of Qingdao, North China, *Sci. Total  
552 Environ.*, 778, 10.1016/j.scitotenv.2021.146265, 2021b.

553 Lu, X., Zhang, L., Wang, X., Gao, M., Li, K., Zhang, Y., Yue, X., and Zhang, Y.: Rapid Increases in Warm-Season Surface Ozone  
554 and Resulting Health Impact in China Since 2013, *Environ. Sci. Tech. Lett.*, 7, 240-247, 10.1021/acs.estlett.0c00171, 2020.

555 Marley, N. A., Gaffney, J. S., Ramos-Villegas, R., and ' , B. C. G.: Comparison of measurements of peroxyacyl nitrates and primary  
556 carbonaceous aerosol concentrations in Mexico City determined in 1997 and 2003, *Atmos. Chem. Phys.*, 7, 2277-2285, 2007a.

557 Marley, N. A., Gaffney, J. S., Ramos-Villegas, R., and Gonzalez, B. C.: Comparison of measurements of peroxyacyl nitrates and  
558 primary carbonaceous aerosol concentrations in Mexico City determined in 1997 and 2003, *Atmos. Chem. Phys.*, 7, 2277–  
559 2285, 2007b.

560 Pratap, V., Carlton, A. G., Christiansen, A. E., and Hennigan, C. J.: Partitioning of ambient organic gases to inorganic salt solutions:  
561 influence of salt identity, ionic strength, and pH, *Geophys. Res. Lett.*, 48, 10.1029/2021gl095247, 2021.

562 Roberts, J. M., Flocke, F., Stroud, C. A., Hereid, D., Williams, E., Fehsenfeld, F., Brune, W., Martinez, M., and Harder, H.: Ground-  
563 based measurements of peroxy-carboxylic nitric anhydrides (PANs) during the 1999 Southern Oxidants Study Nashville  
564 Intensive, *J Geophys Res-Atmos*, 107, ACH 1-1-ACH 1-10, 10.1029/2001jd000947, 2002.

565 Senum, G. I., Fajer, R., & Gaffney, J. S. Fourier transform infrared spectroscopic study of the thermal stability of peroxyacetyl  
566 nitrate, *J. Phys. Chem.*, 90, 152-156, 10.1021/j100273a034, 1986.

567 Sun, M., Cui, J. n., Zhao, X., and Zhang, J.: Impacts of precursors on peroxyacetyl nitrate (PAN) and relative formation of PAN to  
568 ozone in a southwestern megacity of China, *Atmos. Environ.*, 231, 10.1016/j.atmosenv.2020.117542, 2020.

569 Sun, M., Zhou, Y., Wang, Y., Qiao, X., Wang, J., and Zhang, J.: Heterogeneous reaction of peroxyacetyl nitrate on real-world PM<sub>2.5</sub>

570 aerosols: Kinetics, influencing Factors, and atmospheric implications, *Environ. Sci. Tech.*, 56, 9325-9334,  
571 10.1021/acs.est.2c03050, 2022.

572 Taylor, O. C.: Importance of peroxyacetyl nitrate (PAN) as a phytotoxic air pollutant, *J. Air Pollut. Control Assoc.*, 19, 347-351,  
573 10.1080/00022470.1969.10466498, 1969.

574 Tuazon, E. C., Carter, W. P., & Atkinson, R. : Thermal decomposition of peroxyacetyl nitrate and reactions of acetyl peroxy radicals  
575 with nitric oxide and nitrogen dioxide over the temperature range 283-313 K. *J. Phys. Chem.*, 95, 2434-2437,  
576 10.1021/j100159a059, 1991.

577 Wang, B., Shao, M., Roberts, J. M., Yang, G., Yang, F., Hu, M., Zeng, L., Zhang, Y., and Zhang, J.: Ground-based on-line  
578 measurements of peroxyacetyl nitrate (PAN) and peroxypropionyl nitrate (PPN) in the Pearl River Delta, China. , *Int. J.*  
579 *Environ. Anal. Chem.*, 90, 548–559, 10.1080/03067310903194972, 2010.

580 Wang, H., Lyu, X., Guo, H., Wang, Y., Zou, S., Ling, Z., Wang, X., Jiang, F., Zeren, Y., Pan, W., Huang, X., and Shen, J.: Ozone  
581 pollution around a coastal region of South China Sea: interaction between marine and continental air, *Atmos. Chem. Phys.*, 18,  
582 4277-4295, 10.5194/acp-18-4277-2018, 2018.

583 Wang, Y., Liu, T., Gong, D., Wang, H., Guo, H., Liao, M., Deng, S., Cai, H., and Wang, B.: Anthropogenic pollutants induce changes  
584 in peroxyacetyl nitrate formation intensity and pathways in a mountainous background atmosphere in southern China, *Environ.*  
585 *Sci. Tech.*, 10.1021/acs.est.2c02845, 2023.

586 Wu, X., Xu, L., Hong, Y., Chen, J., Qiu, Y., Hu, B., Hong, Z., Zhang, Y., Liu, T., Chen, Y., Bian, Y., Zhao, G., Chen, J., and Li, M. :  
587 The air pollution governed by subtropical high in a coastal city in Southeast China: Formation processes and influencing  
588 mechanisms, *Sci. Total Environ.*, 692, 1135-1145, 10.1016/j.scitotenv.2019.07.341, 2019.

589 Xu, W., Zhang, G., Wang, Y., Tong, S., Zhang, W., Ma, Z., Lin, W., Kuang, Y., Yin, L., and Xu, X.: Aerosol promotes peroxyacetyl  
590 nitrate formation during winter in the North China Plain, *Environ. Sci. Technol.*, 55, 3568-3581, 10.1021/acs.est.0c08157, 2021.

591 Xu, X., Zhang, H., Lin, W., Wang, Y., Xu, W., and Jia, S.: First simultaneous measurements of peroxyacetyl nitrate (PAN) and ozone  
592 at Nam Co in the central Tibetan Plateau: impacts from the PBL evolution and transport processes, *Atmos. Chem. Phys.*, 18,  
593 5199-5217, 10.5194/acp-18-5199-2018, 2018.

594 Xu, Z., Xue, L., Wang, T., Xia, T., Gao, Y., Louie, P. K. K., and Luk, C. W. Y.: Measurements of peroxyacetyl nitrate at a background  
595 site in the Pearl River Delta region: production efficiency and regional transport, *Aerosol Air Qual. Res.*, 15, 833-841,  
596 10.4209/aaqr.2014.11.0275, 2015.

597 Xue, L., Wang, T., Wang, X., Blake, D. R., Gao, J., Nie, W., Gao, R., Gao, X., Xu, Z., Ding, A., Huang, Y., Lee, S., Chen, Y., Wang,  
598 S., Chai, F., Zhang, Q., and Wang, W.: On the use of an explicit chemical mechanism to dissect peroxy acetyl nitrate formation,  
599 *Environ. Pollut.*, 195, 39-47, 10.1016/j.envpol.2014.08.005, 2014.

600 Xue, L. K., Wang, T., Guo, H., Blake, D. R., Tang, J., and Zhang, X. C.: Sources and photochemistry of volatile organic compounds



601 in the remote atmosphere of western China: results from the Mt. Waliguan Observator, *Atmos. Chem. Phys.*, 13, 8551-8567,  
602 10.5194/acp-13-8551-2013, 2013.

603 Yang, X., Wu, K., Wang, H., Liu, Y., Gu, S., Lu, Y., Zhang, X., Hu, Y., Ou, Y., Wang, S., and Wang, Z.: Summertime ozone pollution  
604 in Sichuan Basin, China: Meteorological conditions, sources and process analysis, *Atmos. Environ.*, 226,  
605 10.1016/j.atmosenv.2020.117392, 2020.

606 Ye, C., Zhang, N., Gao, H., and Zhou, X.: Photolysis of particulate nitrate as a source of HONO and NO<sub>x</sub>, *Environ. Sci. Technol.*,  
607 51, 6849-6856, 10.1021/acs.est.7b00387, 2017.

608 Yuan, J., Ling, Z., Wang, Z., Lu, X., Fan, S., He, Z., Guo, H., Wang, X., and Wang, N.: PAN-precursor relationship and process  
609 analysis of PAN variations in the Pearl River Delta region, *Atmos.*, 9, 10.3390/atmos9100372, 2018.

610 Yukihiro, M., Hiramatsu, T., Bouteau, F., Kadono, T., and Kawano, T.: Peroxyacetyl nitrate-induced oxidative and calcium signaling  
611 events leading to cell death in ozone-sensitive tobacco cell-line, *Plant Signal Behav.*, 7, 113-120, 10.4161/psb.7.1.18376, 2012.

612 Zeng, L., Fan, G. J., Lyu, X., Guo, H., Wang, J. L., and Yao, D.: Atmospheric fate of peroxyacetyl nitrate in suburban Hong Kong  
613 and its impact on local ozone pollution, *Environ. Pollut.*, 252, 1910-1919, 10.1016/j.envpol.2019.06.004, 2019.

614 Zhai, S., Jacob, D. J., Franco, B., Clarisse, L., Coheur, P., Shah, V., Bates, K. H., Lin, H., Dang, R., Sulprizio, M. P., Huey, L. G.,  
615 Moore, F. L., Jaffe, D. A., and Liao, H.: Transpacific transport of Asian peroxyacetyl nitrate (PAN) observed from satellite:  
616 implications for ozone, *Environ. Sci. Tech.*, 58, 9760-9769, 10.1021/acs.est.4c01980, 2024.

617 Zhang, G., Mu, Y., Zhou, L., Zhang, C., Zhang, Y., Liu, J., Fang, S., and Yao, B.: Summertime distributions of peroxyacetyl nitrate  
618 (PAN) and peroxypropionyl nitrate (PPN) in Beijing: Understanding the sources and major sink of PAN, *Atmos. Environ.*, 103,  
619 289-296, 10.1016/j.atmosenv.2014.12.035, 2015.

620 Zhang, J., Guo, Y., Qu, Y., Chen, Y., Yu, R., Xue, C., Yang, R., Zhang, Q., Liu, X., Mu, Y., Wang, J., Ye, C., Zhao, H., Sun, Q., Wang,  
621 Z., and An, J.: Effect of potential HONO sources on peroxyacetyl nitrate (PAN) formation in eastern China in winter, *J. Environ.*  
622 *Sci. (China)*, 94, 81-87, 10.1016/j.jes.2020.03.039, 2020.

623 Zhang, J. M., Wang, T., Ding, A. J., Zhou, X. H., Xue, L. K., Poon, C. N., Wu, W. S., Gao, J., Zuo, H. C., Chen, J. M., Zhang, X.  
624 C., and Fan, S. J.: Continuous measurement of peroxyacetyl nitrate (PAN) in suburban and remote areas of western China,  
625 *Atmos. Environ.*, 43, 228-237, 10.1016/j.atmosenv.2008.09.070, 2009.

626 Zhu, J., Wang, S., Wang, H., Jing, S., Lou, S., Saiz-Lopez, A., and Zhou, B.: Observationally constrained modeling of atmospheric  
627 oxidation capacity and photochemical reactivity in Shanghai, China, *Atmos. Chem. Phys.*, 20, 1217-1232, 10.5194/acp-20-  
628 1217-2020, 2020.

629  
630